LIFE SCIENCES

CTR9 drives osteochondral lineage differentiation of human mesenchymal stem cells via epigenetic regulation of BMP-2 signaling

Ngai Ting Chan[1], Ming-Song Lee[2], Yidan Wang[1], Jacques Galipeau[3], Wan-Ju Li[2], Wei Xu[1]*

Cell fate determination of human mesenchymal stem/stromal cells (hMSCs) is precisely regulated by lineage-specific transcription factors and epigenetic enzymes. We found that CTR9, a key scaffold subunit of polymerase-associated factor complex (PAFc), selectively regulates hMSC differentiation to osteoblasts and chondrocytes, but not to adipocytes. An in vivo ectopic osteogenesis assay confirmed the essentiality of CTR9 in hMSC-derived bone formation. CTR9 counteracts the activity of Enhancer Of Zeste 2 (EZH2), the epigenetic enzyme that deposits H3K27me3, in hMSCs. Accordingly, CTR9 knockdown (KD) hMSCs gain H3K27me3 mark, and the osteogenic differentiation defects of CTR9 KD hMSCs can be partially rescued by treatment with EZH2 inhibitors. Transcriptome analyses identified bone morphology protein–2 (BMP-2) as a downstream effector of CTR9. BMP-2 secretion, membrane anchorage, and the BMP-SMAD pathway were impaired in CTR9 KD MSCs, and the effects were rescued by BMP-2 supplementation. This study uncovers an epigenetic mechanism engaging the CTR9–H3K27me3–BMP-2 axis to regulate the osteochondral lineage differentiation of hMSCs.

INTRODUCTION

Human mesenchymal stem cells (hMSCs), also known as mesenchymal stromal cells, are initially isolated from the bone marrow. MSCs comprise a heterogeneous population of stem cells and lineage commitment progenitors that also reside in other organs and tissues, such as adipose, umbilical cord, and pancreas (*1*, *2*). MSCs are multipotent and express common cell surface markers such as CD73, CD90, and CD105. Under appropriate stimuli, MSCs can differentiate into mesodermal lineage cell types, including osteoblasts, adipocytes, and chondrocytes, and transdifferentiate into ecto/endoderm lineages at a much lower frequency (*3*). Although MSCs can be induced to defined lineages in vitro, the in vivo differentiation of MSCs into adipocytes or osteoblasts/chondrocytes is context dependent and affected by pathological conditions, such as obesity, osteosarcoma, osteoporosis, and chondrodysplasia (*4*, *5*). Therefore, a mechanistic understanding of osteo/chondrogenic and adipogenic differentiation of MSCs could provide molecular basis for designing new treatments for bone/cartilage- and adipose-related diseases.

MSC lineage specification is typically controlled by lineage-specific transcription factors (TFs). For example, the osteogenic differentiation of MSCs is regulated by two master regulators, RUNX2 and Osterix, which sequentially activate osteo-promoting signaling pathways, such as transforming growth factor–β (TGF-β) and Wingless-related integration site (Wnt) /β-catenin (*6*). Furthermore, numerous bone matrix protein coding genes, such as osteopontin and osteocalcin, are target genes of RUNX2 and Osterix (*7*, *8*). In addition to induce osteogenic differentiation, RUNX2 and Osterix inhibit the differentiation of MSCs toward the adipogenic lineage by restraining the expression of PPARγ (peroxisome proliferator–activated receptor γ) and C/EBPα (CCAAT/enhancer binding protein CCAAT/enhancer binding protein), which are the master TFs regulating adipogenesis (*9*). Thus, osteochondral and adipogenesis-specific TFs dictate an interlinked regulatory network, and the induction of one lineage often comes at the expense of the other.

Bone morphogenetic proteins (BMPs) are members of the TGF-β superfamily (*10*) involved in different phases of bone formation, including endochondral ossification and intramembranous ossification (*11*, *12*). Among BMPs, BMP-2 is a potent cartilage and bone inducer. The osteogenic effects of BMP-2 are mediated through the formation of canonical SMAD complexes (SMAD1/5/8; SMAD4), which further activate the transcription of genes involved in osteoblastic/chondrogenic differentiation and bone/cartilage formation, including *RUNX2*, *OSX*, *DLX5*, and *SOX9* (*13*–*15*). The studies on vertebrate skeleton development in vivo also support roles of BMP-2 in regulating bone development and tissue homeostasis. Osteoblast-specific BMP-2 knockout mice (*Sp7*-Cre; *BMP-2*$^{fx/fx}$) elicit defects in osteoblast formation, long bone stiffness, and endochondral fracture healing (*16*–*18*). Concomitantly, BMP-2 is a potent chondrogenic growth factor for cartilage tissue engineering. Activation of p38–mitogen-activated protein kinase signaling by BMP-2 stabilizes SOX9 and stimulates SOX9 expression, thus promoting chondrogenesis (*19*). As a consequence, BMP-2 is the only osteoinductive growth factor approved by U.S. Food and Drug Administration (FDA) for bone healing (*20*–*23*) and various BMP-2 delivery methods are under active investigation for bone repair and regeneration (*24*, *25*).These studies underscore the importance of BMP-2 in osteogenesis and its potential synergism with other osteogenic transcriptional factors.

Lineage-priming TFs interact with epigenetic enzymes to establish distinct epigenetic states, adding another layer of complexity to the transcriptional regulation of MSC lineage-specific differentiation. For instance, activation of RUNX2 requires KDM6A to erase H3K27me3 (*26*), a repressive marker involved in lineage-specific

[1]McArdle Laboratory for Cancer Research, Wisconsin Institute for Medical Research, University of Wisconsin Carbone Comprehensive Cancer Center, Madison, WI 53706, USA. [2]Department of Orthopedics and Rehabilitation, School of Medicine and Public Health, University of Wisconsin-Madison, Madison, WI 53706, USA. [3]Department of Medicine, School of Medicine and Public Health, University of Wisconsin-Madison, Madison, WI 53706, USA.
*Corresponding author. Email: wxu@oncology.wisc.edu

differentiation. For example, osteogenic genes, *RUNX2* and *OPN*, are repressed by EZH2/H3K27me3 (*27*, *28*), whereas H3K27me3 demethylase KDM6A activates *SOX9* and *COL2A1*, thus promoting chondrogenic differentiation (*29*). EZH2 and KDM6A elicit opposing effects on MSCs osteogenic and adipogenic differentiation. The exogenous expression of EZH2 in MSCs promotes adipogenic and inhibits osteogenic differentiation. In contrast, overexpression of KDM6A promotes osteogenic and inhibits adipogenic differentiation (*30*–*32*). Therefore, lineage-specific TFs and epigenetic modulators coordinate to define the lineage specification of MSCs.

CTR9 is the scaffold protein of polymerase-associated factor complex (PAFc) regulating multiple phases of transcription (*33*). CTR9/PAFc was previously shown to regulate lineage-specific genes that are required for mammalian preimplantation development, such as *EOMES*, *ELF5*, and *SOX2*, through modulating H3K36me3 deposition (*34*). CTR9 has been shown to regulate the pluripotency of mouse and human embryonic stem cells (*35*, *36*). Moreover, genome-wide association studies identified *CTR9* as a candidate gene involved in the development of osteoporosis-related Kashin-Beck disease, implicating CTR9 in maintaining bone homeostasis (*37*). We had reported the role of CTR9 to restrain H3K27me3 expansion on chromatin by regulating Polycomb repressive complex 2 (PRC2) subtype equilibrium and KDM6A expression in breast cancer cells (*38*). Given that the PRC2-H3K27me3-KDM6A axis is critical in lineage commitment of hMSCs, we posit that CTR9 may regulate lineage differentiation of hMSCs via an epigenetic mechanism.

In this study, we used loss- and gain-of-function approaches to study the roles of CTR9 in hMSCs maintenance and multifaceted lineage-oriented differentiation. Our studies revealed essential functions of CTR9 in osteochondral but not adipogenic differentiation through regulating BMP-2 expression. Furthermore, the osteogenic differentiation of hMSCs regulated by CTR9 engages in PRC2-H3K27me3 axis. Our findings underscore the functional significance of CTR9 in orchestrating epigenetic enzymes and lineage-specific TFs to promote bone/cartilage formation.

RESULTS

CTR9 depletion has minor effects on the viability and stem cell properties of hMSCs

To examine the functional roles of CTR9 in lineage specification of hMSCs, we first generated hMSC lines stably expressing two distinct CTR9-targeting short hairpin RNAs (shRNAs), with a scramble shRNA serving as a negative control (i.e., shControl versus shCTR9#3 or #5). Western blotting (WB) results confirmed the depletion of CTR9 in hMSCs derived from different donors (H01/H03/H18) at early passages (p3/p4) (Fig. 1A). CTR9 knockdown (KD) in hMSCs resulted in a notable morphology change measured by immunofluorescent staining of the cytoskeleton (F-actin/β-tubulin) (Fig. 1B). In contrast to the fibroblast-like morphology of shControl MSCs, CTR9 KD cells were enlarged and branched, accompanied by the decreased cell-cell adhesion. Despite the morphological changes, cell survival was moderately affected. The flow cytometry analysis of propidium iodide (PI)/annexin V uptake showed a mild increase of apoptotic cells (PI^-/annexin-V^+) after CTR9 depletion, whereas the necrotic cells (PI^+/annexin-V^+) were not evident in either shControl or shCTR9 hMSCs. Apoptosis and necrosis were induced in parental hMSCs using hydrogen peroxide (H_2O_2), serving as a positive control (Fig. 1C) (*39*). The effect of CTR9 KD on viability of hMSCs was also measured using a duo-fluorescence–based cell cytotoxicity assay. Both control KD and CTR9 KD hMSCs remain largely viable as illustrated by high intracellular esterase activity (bright green) and intact plasma membrane integrity (deem red) (*40*). This contrasts with massive cell death when hMSCs undergone formaldehyde fixation, serving as a positive control (fig. S1A). To further delineate the effect of CTR9 depletion on hMSCs, we detected the expression of cellular markers of proliferation, senescence, and stress granules by WB (Fig. 1D). The results showed a substantial decrease of Ki67 and proliferating cell nuclear antigen upon CTR9 KD. On the contrary, the expression of senescence markers (p16INK4α and β-galactosidase) and stress granules components (G3BP1/PABP1) that moderately increased in response to CTR9 depletion as compared to positive control of parental hMSCs underwent a 2-day serum starvation followed by treatment with sodium arsenite (*41*). Serum-starved, sodium arsenite–treated hMSCs expressed higher levels of senescence and stress granule–associated proteins but lower proliferative marker proteins as compared to CTR9 KD hMSCs. These results agree with the moderate increase of senescence-associated β-galactosidase in CTR9 KD hMSCs (fig. S1B) and increase of hMSCs in G_0-G_1 phase of the cell cycle (Fig. 1E). Immunofluorescence staining of Ki67, β-galactosidase and G3BP1 in control KD, two CTR9 KD clones, and pretreated parental hMSCs reinforced the minor effect of CTR9 in regulation of proliferation, cell stress, and senescence phenotypes of hMSCs (Fig. 1F).

We next compared the three-dimensional (3D) spheroid formation and stem cell marker expression between shControl and shCTR9 hMSCs. The depletion of CTR9 did not affect the 3D spheroid formation (Fig. 1G) nor the viability and integrity of cell aggregates (labeled with CellTracker Green and phalloidin) (fig. S1C). Furthermore, CTR9 KD did not result in significant changes on the expression of MSC surface markers and other pluripotency regulatory genes (Fig. 1H). In summary, although CTR9 KD moderately affected the morphology and proliferation of hMSCs, the viability and stem cell properties of hMSCs were not remarkably affected by the loss of CTR9.

KD of CTR9 in hMSCs impairs sequential osteogenic differentiation

We next investigated whether depletion of CTR9 affects the lineage specification of hMSCs. Several studies implicated that CTR9 level is likely associated with osteogenic potential (*36*, *42*). Thus, we compared shControl and shCTR9#3/#5 MSCs in the in vitro osteogenic assays. The hMSCs were treated with osteogenic induction medium for 28 days, during which osteogenic markers were sequentially measured at different time points (Fig. 2A). The alkaline phosphatase (ALP) activity indicates the presence of osteoprogenitor or osteoblast cells (*43*). In Fig. 2B, shControl MSCs elicited much stronger ALP activity just 7-days after osteogenic induction as compared with shCTR9 hMSCs. The quantification of ALP activity normalized by DNA content was also shown in Fig. 2B (right). In addition to ALP activity, increased collagen level stained by Picrosirius red is another marker of osteogenesis. In fig. S2A, the strong red staining of collagen fibers was observed in shControl, but not in shCTR9 hMSCs, after 28-day osteogenic induction. Given that elevated ALP activity and enhanced collagen synthesis/secretion are

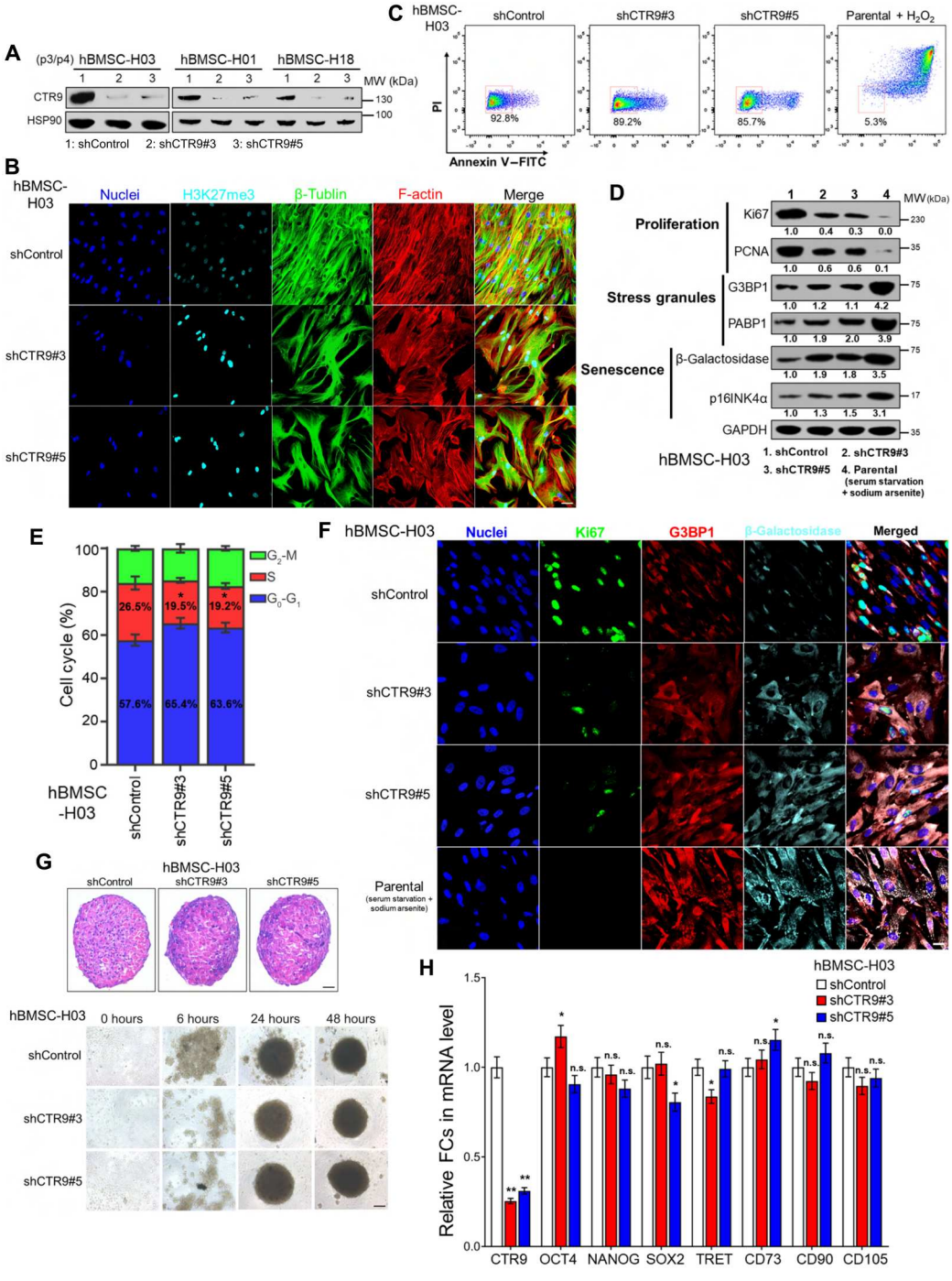

Fig. 1. CTR9 KD has minor effects on viability, morphology, and proliferation of hMSCs. (**A**) CTR9 levels in two CTR9 KD early-passage (p3/p4) clones of hMSCs derived from three donors as compared withhMSCs expressing shControl. β-Actin served as a loading control. MW, molecular weight; hBMSCs, human bone marrow-derived mesenchymal stem/stomal cells. (**B**) Immunofluorescence staining of nuclei (blue), F-actin (red), β-tubulin (green), and H3K27me3 (cyan) in shControl and shCTR9 hMSCs . Scale bar, 40× (applied to all images). (**C**) Flow cytometry of PI staining and annexin-V–fluorescein isothiocyanate (FITC) of shControl and two shCTR9 hMSC lines. Hydrogen peroxide (H_2O_2) served as a positive control. (**D**) WB of indicated proteins in shControl, shCTR9 hMSCs, and serum-starved hMSCs treated with sodium arsenite. The bands' intensities were normalized with glyceraldehyde-3-phosphate dehydrogenase (GAPDH). PCNA, proliferating cell nuclear antigen; (**E**) Cell cycle profiles of shControl or shCTR9 hMSCs. Data are represented as means ± SD ($n = 3$). *P* values were calculated by two-tailed *t* test (*$P < 0.05$). (**F**) Immunofluorescence staining of Ki67 (green), G3BP1 (red), β-galactosidase (cyan), and nuclei (Hoechst 33342) in shControl and shCTR9 hMSCs. Parental hMSCs were treated as in (D). Scale bar, 60× (applied to all images). (**G**) Top: Representative hematoxyin and eosin (H&E) staining of 3D spheroids of shControl or shCTR9 hMSCs 72 hour after seeding. Bottom: Representative images of 3D spheroids by equal numbers of shControl or shCTR9 hMSCs after seeding at indicated time. Scale bar, 10× (at the bottom right applied to all images). (**H**) Reverse transcription quantitative polymerase chain reaction analyses of CTR9, stemness genes (OCT4/NANOG/SOX2/TRET), and MSC-specific surface antigens (CD73/CD90/CD105) in shControl and shCTR9 hMSCs. Relative fold change (FC) in mRNA levels is represented as means ± SD ($n = 3$) and were normalized to β-actin. *P* values were calculated by two-tailed *t* test (*$P < 0.05$; n.s., not significant).

hallmarks of osteogenesis and are a prerequisite for calcium-enriched extracellular matrix (ECM) formation, we conclude that CTR9 KD impedes osteogenic differentiation of hMSCs.

Second, we measured the calcium mineralization in ECM, as it distinguishes a terminally differentiated osteoblast from a premature one. Mature osteoblasts secrete large amounts of collagen-proteoglycan matrix, which binds calcium salts [mainly hydroxyapatite, Ca5(PO4)3(OH)] during osteogenesis (*44*). As expected, shControl, but not shCTR9 hMSCs, formed substantial amounts of mineralized calcium matrix after 28 days of osteoinduction as shown by Alizarin Red S staining and quantification (Fig. 2C). The defects of ALP activity and calcium-mineralized ECM formation in shCTR9 hMSCs could be observed in hMSCs derived from different donors (H01/H18) (fig. S2, B and C).

Third, we quantified the secretion of osteoglycoproteins or γ-carboxyglutamic acid–containing calcium-binding proteins including osteocalcin/osteonectin/osteopontin, another marker of osteogenesis (*45*, *46*). To determine whether CTR9 depletion affects the

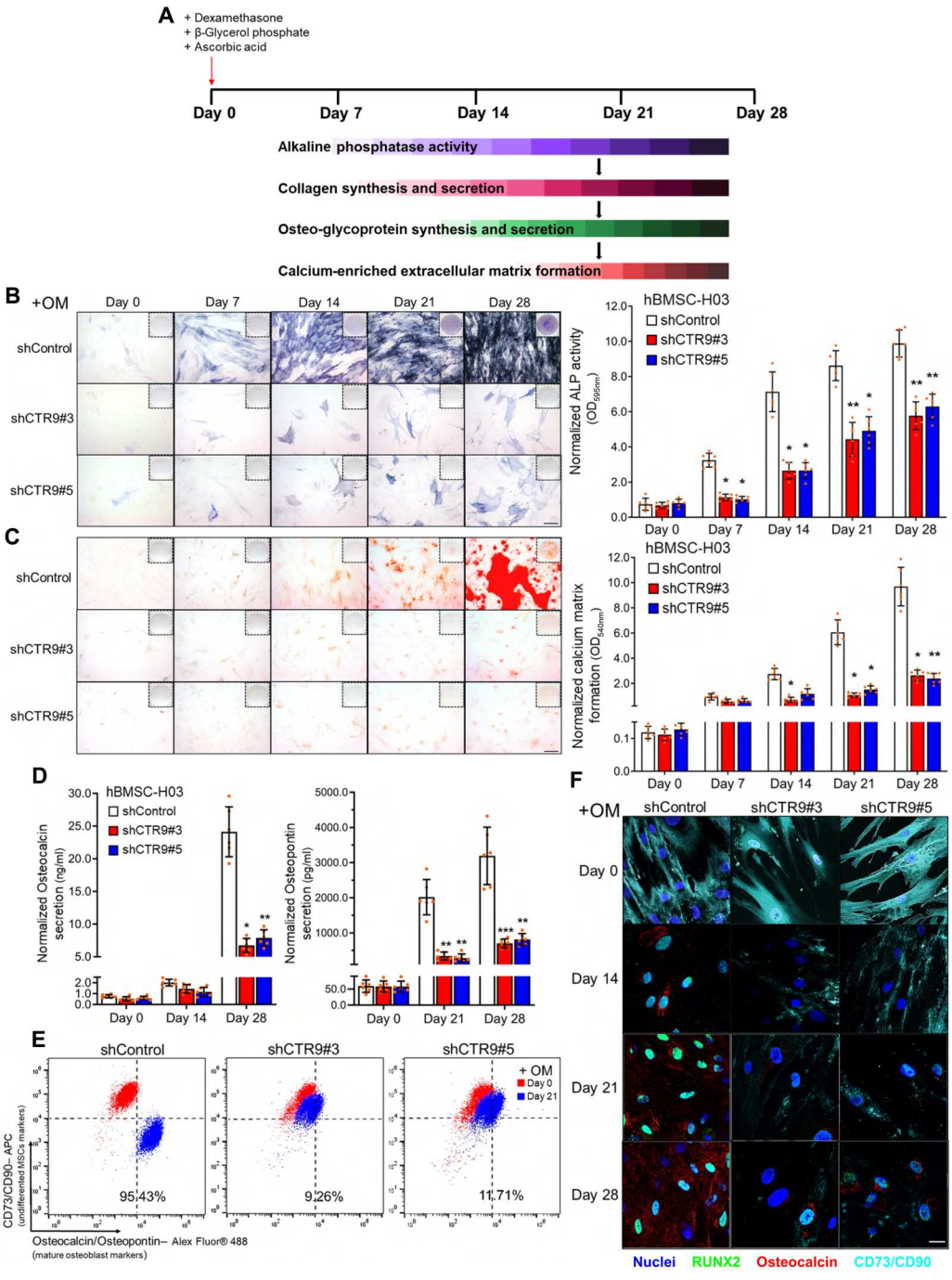

Fig. 2. Osteogenic differentiation was impaired in CTR9 KD hMSCs. (**A**) Schematic workflow of osteogenic induction of hMSCs in vitro. (**B**) Left: Representative images showing the ALP activity–associated BCIP-NBT staining (violet blue) in shControl or shCTR9 hMSCs (shCTR9#3/#5) from days 0 to 28 of osteogenic induction. Scale bar, 20× (at the bottom right applied to all corresponding images). Right: Quantification of ALP activity by optical density at 595 nm (OD_{595nm}) absorbance normalized with respective DNA content. Data are represented as means ± SD ($n = 3$). *P* values were calculated by two-tailed *t* test with $*P < 0.05$ and $**P < 0.01$. OM, osteogenic induction medium. (**C**) Left: Representative images showing the calcium matrix formation stained with Alizarin Red S of shControl or shCTR9 hMSCs (shCTR9#3/#5) from days 0 to 28 of osteogenic induction. Scale bar, 20× (at the bottom right applied to all corresponding images). Right: Quantification of ECM formation by OD_{540nm} absorbance normalized with the respective DNA content. Data are represented as means ± SD ($n = 3$). *P* values were calculated by two-tailed *t* test with $*P < 0.05$ and $**P < 0.01$. (**D**) Osteocalcin (left) and Osteopontin (right) secretion of shControl or shCTR9 hMSCs (shCTR9#3/#5) measured using the human Osteocalcin/Osteopontin enzyme-linked immunosorbent assay (ELISA) kit after 0, 14, or 28 days of osteogenic induction followed by 2-day culture in serum-free medium. Data normalized by the respective DNA content are represented as means ± SD ($n = 6$). *P* values were calculated by two-tailed *t* test with $*P < 0.05$, $**P < 0.01$ and $***P < 0.001$. (**E**) Flow cytometry analyses of CD73/CD90, the undifferentiated hMSCs markers, and Osteocalcin/Osteopontin, the osteogenic differentiated hMSCs markers, in shControl or shCTR9 hMSCs (shCTR9#3/#5) on days 0 and 21 of osteogenic induction. (**F**) Immunofluorescence imaging of CD73/CD90 (cyan), RUNX2 (green), and Osteocalcin in shControl or shCTR9 hMSCs (shCTR9#3/#5) from days 0 to 28 of osteogenic induction. Nuclei were stained by Hoechst 33342 in blue.

secretion of these osteo-specific ECM proteins, we performed enzyme-linked immunosorbent assay (ELISA) for secreted human specific osteocalcin and osteopontin after shControl, and shCTR9 hMSCs were induced for 0, 14, 21, and 28 days. The result showed that CTR9 depletion significantly reduced osteocalcin/osteopontin secretion after 14- or 28-day in vitro osteoinduction (Fig. 2D).

Last, we assessed the osteogenic efficiency by quantifying undifferentiated MSC markers CD73/CD90 and osteogenic markers osteocalcin/osteopontin using flow cytometry after 21-day osteogenic induction. shControl hMSCs, but not shCTR9 hMSCs, displayed increased osteocalcin/osteopontin and decreased CD73/CD90 expression (Fig. 2E). This result was substantiated by immunofluorescence staining of CD73/CD90 and osteoblast-specific proteins RUNX2 and osteocalcin (Fig. 2F). A substantial increase of

RUNX2 expression (green) was observed between 14 and 21 days of osteogenic induction in the shControl group. Similarly, immunofluorescence staining detected initial osteocalcin synthesis near the endoreticulum (ER) on day 14 and accumulation of osteocalcin on day 28 of osteogenic differentiation, accompanied by the reduction of CD73/CD90 expression. shCTR9 MSCs exhibited delayed RUNX2 expression or osteocalcin synthesis while maintaining the expression of undifferentiated surface markers, CD73/CD90, indicating a blockade of hMSC osteogenesis. The impaired osteogenesis in CTR9 KD hMSCs were further validated by reverse transcription quantitative polymerase chain reaction (RT-qPCR) (fig. S2D) and immunofluorescence staining (fig. S2E) of respective markers during 14 to 28 days of osteogenic induction of hMSCs. All data (i.e., reduced collagen fibrosis, ECM osteo-protein secretion, and decreased expression of osteoblast markers) support the notion that the loss of CTR9 strongly impedes osteogenic differentiation, underscoring the essential role of CTR9 in the osteogenic lineage determination of hMSCs.

The expression levels of CTR9 are associated with osteogenic potential

Given that knocking down CTR9 impairs the osteogenic potential of hMSCs, we next investigated whether the osteogenic potential of hMSCs is CTR9 dose dependent. Flag-tagged CTR9 was exogenously expressed in shControl or shCTR9 hMSCs. WB results showed the restoration of CTR9 protein in shCTR9 hMSCs, and CTR9 is overexpressed in shControl hMSCs (Fig. 3A). When CTR9 expression was restored to the same levels of the parental hMSCs, the osteogenic defects were largely alleviated as shown by ALP activity, calcium deposition, and osteocalcin secretion, in comparison to the shCTR9 hMSCs expressing vector control (shCTR9#3/#5 + Flag-CTR9 versus shCTR9#3/#5 + Vector) (Fig. 3, B and C, and fig. S3). Notably, the exogenous expression of CTR9 in shControl hMSCs elevated osteogenic potential as compared with shControl hMSCs expressing blank vector (i.e., shControl + Flag-CTR9 versus shControl + Vector) (Fig. 3, B and C). Together, these data strongly suggest that CTR9 is a bona fide regulator of osteogenesis, and the osteogenic potential of hMSCs is governed by CTR9 levels.

CTR9 is required for in vivo bone formation

The osteogenic defects associated with CTR9 loss in hMSCs in vitro prompted us to investigate the role of CTR9 in modulating MSC-derived bone formation in vivo using an ectopic bone formation assay (Fig. 4A). shControl and shCTR9 hMSCs were seeded on the fused filament fabrication–printed 3D polycaprolactone (PCL) scaffolds at a density of 10^6 cells/cm^3. After 7-day pre-osteodifferentiation in vitro, the shControl and shCTR9 hMSC-containing scaffolds were subcutaneously implanted to the bilateral dorsal surface of immunodeficient mice symmetrically. Mice (n = 4) that were implanted with only scaffold serve as negative controls. The in vivo micro–computed tomography (CT) scanning was performed after 4 to 8 weeks of implantation, followed by harvesting the embedded 3D PCL scaffolds for ex vivo micro-CT scanning, Alizarin Red S staining, and immunostaining of osteogenic markers. The in vivo micro-CT scanning revealed extensive areas of bone matrix–like calcification in scaffolds containing shControl hMSCs after 4 weeks of in vivo implantation, and the mineral density in those areas was further increased after 8-week implantation. In contrast, the scaffolds containing shCTR9 hMSCs exhibited lower levels of calcification and less mineral density as compared with the shControl MSCs after 4 to 8 weeks of implantation (fig. S4A). As expected, the mock group had no detectable signal. The quantification of calcification volume (in mm^3) and the mineral density of the scaffolds (in mg/cm^3) are shown in Fig. 4 (B and C). The ex vivo CT scan results of the scaffolds retrieved from the mice after 8-week implantation agree with those of the in vivo CT scan (fig. S4B). Bromochloroindolyl phosphate–nitro blue tetrazolium (BCIP-NBT) and Alizarin Red S staining of the harvested scaffolds also showed that the scaffolds seeded with shControl hMSCs had significantly higher ALP activity and calcium deposition compared to the shCTR9 counterparts (Fig. 4, D and E). Moreover, decreased osteocalcin sedimentation (green immunofluorescence) across the scaffolds was observed in shCTR9 MSCs as compared to shControl (Fig. 4F), which agrees with the ELISA results (Fig. 4G). Last, hematoxylin and eosin, Von-Kossa, and Masson′s trichome staining of paraffin-embedded scaffold showed the reduced osteoid accretion, calcium deposition, and scaffold mineralization when CTR9 was depleted (Fig. 4, H to J). Moreover, collagen fiber consolidation and ALP activation were compromised in CTR9 KD group as shown by Picrosirius red and ALP staining, respectively (Fig. 4, K and L). Together, our results demonstrate that CTR9 is indispensable for bone formation both in vitro and in vivo.

Loss of CTR9 impairs the chondrogenic differentiation of hMSCs

Chondrogenesis and osteogenesis are being recognized as coupled developmental processes in vivo (*47*). Many signaling pathways and lineage-specific TFs are involved in both processes, such as ALP and RUNX2 (*48*). Because CTR9 depletion impedes osteogenesis in vitro and in vivo, we sought to examine whether CTR9 KD also hinders chondrogenesis. Unlike osteoblasts, chondrocytes can lose their chondrogenic potential and dedifferentiate to osteochondral progenitors in 2D culture conditions (*49*). Therefore, in vitro chondrogenic differentiation uses 3D spherical chondrocyte model (Fig. 5A). After 21 days of in vitro chondrogenic induction, the chondrocyte spheroids were collected for measuring collagens, proteoglycans, glycosaminoglycans (GAGs) and expression of chondrocyte markers. Comparing with shControl spheroids after 14 to 21 days of chondrogenesis, shCTR9 hMSCs exhibited reduced chondrocyte differentiation measured by cartilaginous ECM (CECM) formation using Alcian blue and toluidine blue staining (Fig. 5, B and C) and GAGs using a miniaturized dimethyl-methylene blue (DMMB) assay (Fig. 5, D and E). In addition, collagen production (fig. S5A) and ALP activity (fig. S5B) were compromised in CTR9 KD spheroids after 14 to 21 days of chondrogenic induction. To determine whether genes shared by osteogenesis and chondrogenesis are affected by CTR9 depletion, we extracted RNA from control KD and CTR9 KD spheroids after 21-day chondrogenic induction and quantified the expression of chondrocyte markers by RT-qPCR. The heatmap (fig. S5C) showed that the chondrocyte-associated TFs, including *GLI*, *SOX9*, and *RUNX2*, as well as chondrogenic markers, including *ALPL*, *Col1A1*, *Col2A1*, *Col10A1*, *ACAN*, and *CHAD*, were dramatically decreased upon CTR9 KD. The results were confirmed by multiplex immunofluorescence staining of SOX9, chondroadherin, aggrecan, ALP, and collagen type I/II (Fig. 5F). Collectively, our data underscore the transcriptional regulatory role of CTR9 in osteochondral differentiation.

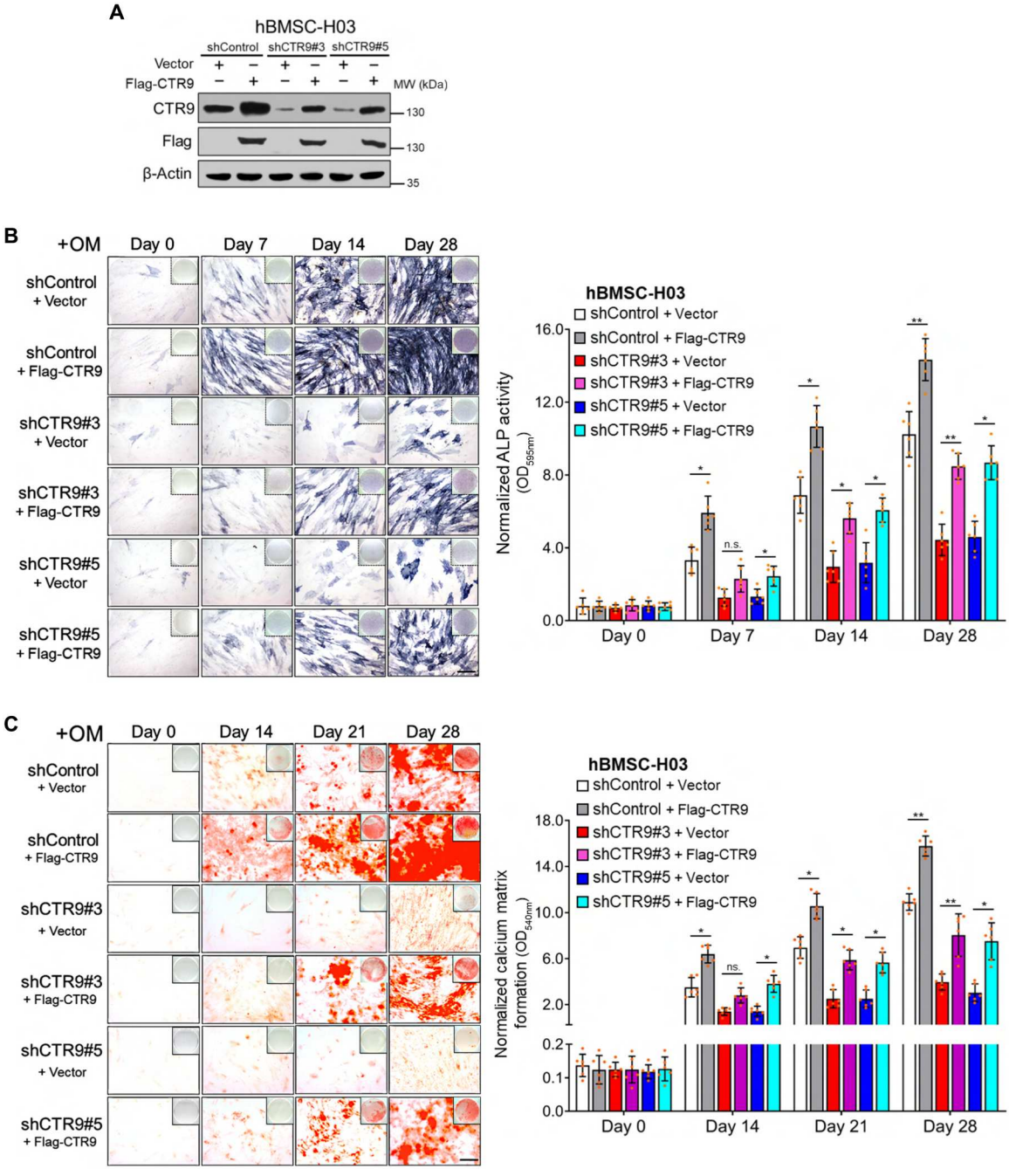

Fig. 3. Osteogenic differentiation potential of hMSCs is CTR9 dose dependent. (**A**) WB analyses of CTR9 levels in shControl or shCTR9 hMSCs (shCTR9#3/#5) exogenously express Flag-CTR9. Blank vectors were transfected as controls (+ Vector). (**B**) Right: Representative images of BCIP-NBT staining (violet blue) of shControl or shCTR9 hMSCs (shCTR9#3/#5) transfected with blank vector (+ Vector) or Flag-CTR9 plasmid (+ Flag-CTR9) from days 0 to 28 of osteogenic induction. Scale bar, 20× (at the bottom right applied to all corresponding images). Left: Quantification of ALP activity by OD_{595nm} absorbance normalized with the respective DNA content. Data are represented as means ± SD ($n = 6$). *P* values were calculated by two-tailed *t* test with $^{*}P < 0.05$ and $^{**}P < 0.01$. (**C**) Right: Representative images showing the ECM formation with Alizarin Red S staining of shControl or shCTR9 hMSCs (shCTR9#3/shCTR9#5) transfected with blank vector (+ Vector) or Flag-CTR9 plasmid (+ Flag-CTR9) from days 0 to 28 of osteogenic induction. Scale bar, 20× (at the bottom right applied to all corresponding images). Left: Quantification of ECM formation by OD_{540nm} absorbance normalized with the respective DNA content. Data are represented as means ± SD ($n = 6$). *P* values were calculated by two-tailed *t* test with $^{*}P < 0.05$ and $^{**}P < 0.01$.

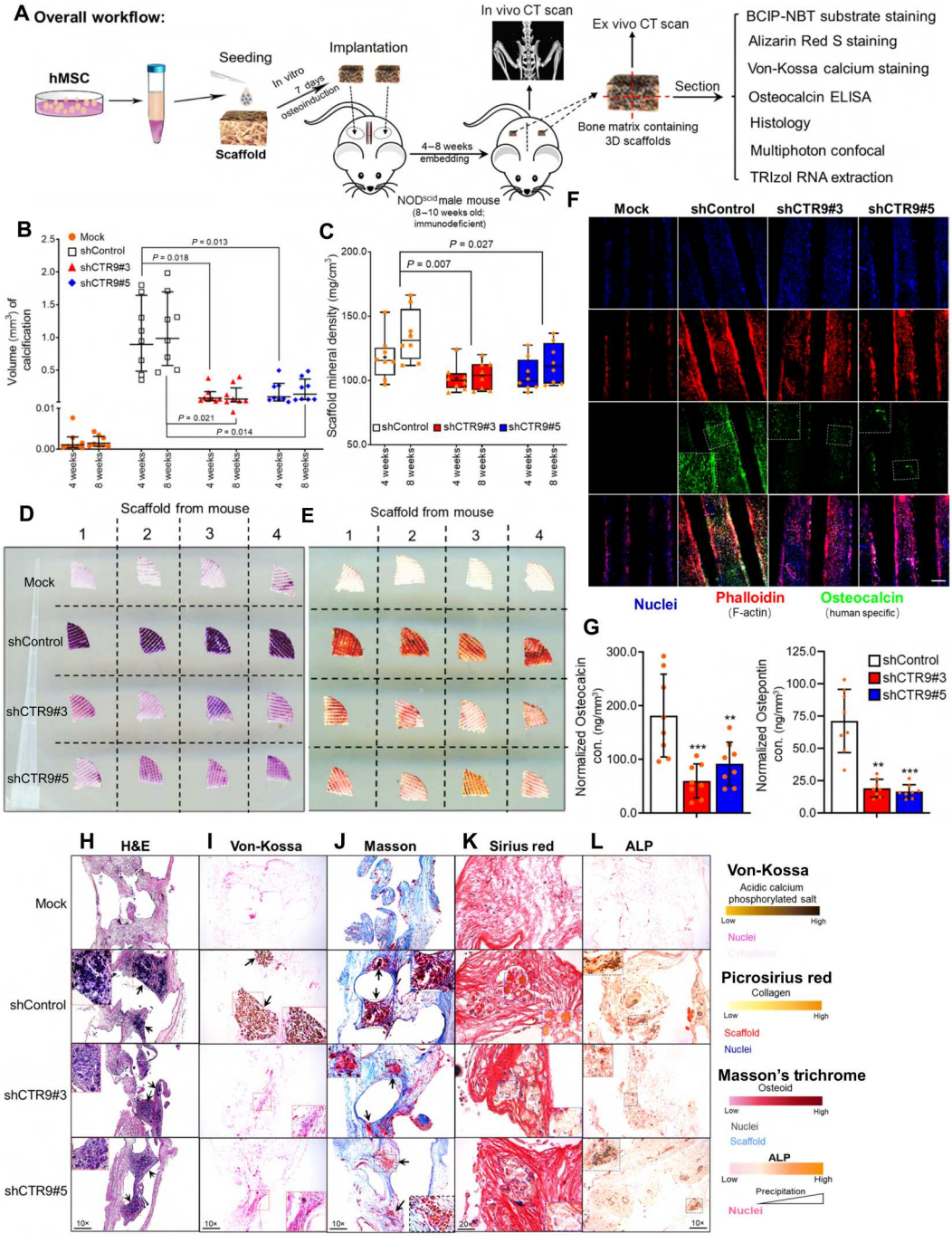

Fig. 4. CTR9 is required for in vivo bone formation. (**A**) Schematic workflow for in vivo ectopic bone formation assay using mock, shControl, and two shCTR9 hMSC lines. (**B**) Scatter dot plot showing the calculated volume (cubic millimeter) of calcification within the implanted 3D scaffolds after micro-CT scanning. Data are depicted as means ± SD ($n = 8$). *P* values that were calculated by two-tailed *t* test with Welch's correction were shown. (**C**) Box plot showing the converted mineral density (milligram per cubic millimeter) of calcification within the implanted 3D scaffolds after in vivo micro-CT scanning. Box and whiskers depict 5th to 95th percentiles, and error lines depict the minimum to maximum box plot ($n = 8$). Mean was labeled with "+." *P* values that were calculated by two-tailed *t* test with Welch's correction were shown. (**D**) ALP activity staining in a quarter of sectioned scaffolds seeded with shControl or shCTR9 hMSCs after 8-week implantation in mice. A 10-μl tip at the left serves as a scale bar in the integral view. (**E**) Calcium matrix deposition staining (Alizarin Red S) of scaffolds described in (D) with the same scale bar. (**F**) Confocal immunofluorescence staining of nuclei (blue), F-actin (red), and osteocalcin (green) of scaffolds described in (D). Scale bar, 10× (applied to all images). (**G**) Quantification of osteocalcin (left) and osteopontin (right) expression by ELISA in scaffolds described in (D). The mock group served as a background control. Data were prenormalized with the respective dry weight of 3D scaffolds and presented as means ± SD ($n = 8$). *P* values were calculated by two-tailed *t* test with Welch's correction (*$P < 0.05$ and **$P < 0.01$). (**H** to **L**) Representative H&E (H), Von-Kossa (I), Masson's trichome (J), Picrosirius red (K), and fast red TR/naphthol AS-MX phosphate staining (for ALP) (L) on scaffolds described in (D). Calcification spots or areas with clustered collagen enrichment or elevated ALP activity were denoted with arrowheads or with zoomed dash boxes, respectively.

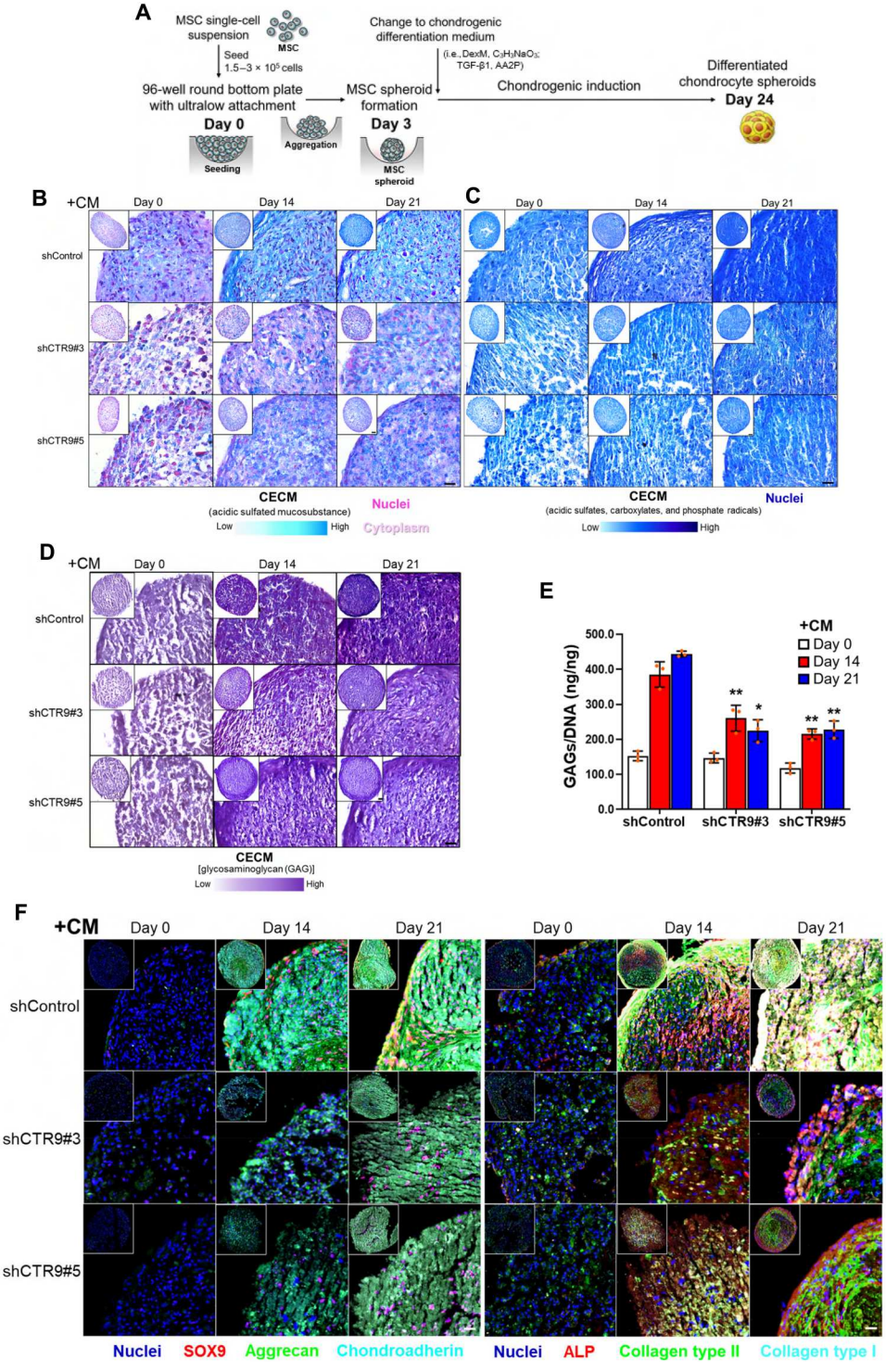

Fig. 5. CTR9 loss impairs chondrogenesis of hMSCs. (**A**) Schematic workflow of chondrogenic induction of hMSCs using 3D spheroid culture model. (**B**) Representative images of Alcian blue (pH 2.5) staining on 3D spheroids of shControl or shCTR9 hMSCs (shCTR9#3/#5) after 0 to 21 days of chondrogenic induction. CECM was stained in light blue. Nuclei were stained in pink, and cytoplasms were stained in pale pink. CM, chondrogenic induction medium. (**C**) Representative images of Toluidine blue staining of 3D spheroids of shControl and shCTR9 hMSCs (shCTR9#3/#5) after 0 to 21 days of chondrogenic induction. CECM was stained in dark blue. Nuclei were stained in violet blue. (**D**) Representative images of DMMB staining of 3D spheroids of shControl and shCTR9 hMSCs (shCTR9#3/#5) after 0 to 21 days of chondrogenic induction. GAGs were stained in dark purple. (**E**) Quantification of GAGs content in 3D spheroids of shControl and shCTR9 hMSCs (shCTR9#3/#5) after 0 to 21 days of chondrogenic induction. Data normalized by the respective DNA content are represented as means ± SD ($n = 3$). *P* values were calculated by two-tailed *t* test with Welch's correction (*$P < 0.05$ and **$P < 0.01$). (**F**) Multiplex immunofluorescence staining of SOX9/aggrecan/chondroadherin (left) and ALP/collagen type II/type I (right) in 3D spheroids of shControl and shCTR9 hMSCs (shCTR9#3/#5) after 0 to 21 days of chondrogenic induction. Nuclei were stained in blue by Hoechst 33342. Scale bar, 60× (at the bottom right applied to all images).

Loss of CTR9 did not alter the adipogenic differentiation of hMSCs

Multipotent hMSCs can differentiate into osteoblast, chondrocyte, and adipocyte lineages. Numerous studies have demonstrated that in vivo lineage determination is under the control of lineage-specific TFs, and promotion of one lineage often comes at the expense of the other. Because the loss of CTR9 results in decreased osteogenic and chondrogenic potential of hMSCs, we next investigated whether CTR9 KD hMSCs are more inclined to differentiate into adipocytes. Using the in vitro adipogenic differentiation for hMSCs (Fig. 6A), lipid droplets can be visible in mature adipocytes, and the neutral triglycerides and other lipids of those vesicles can be stained with Oil Red O after 21 days. Figure 6B showed that comparable levels of lipid vesicles were observed between shControl and

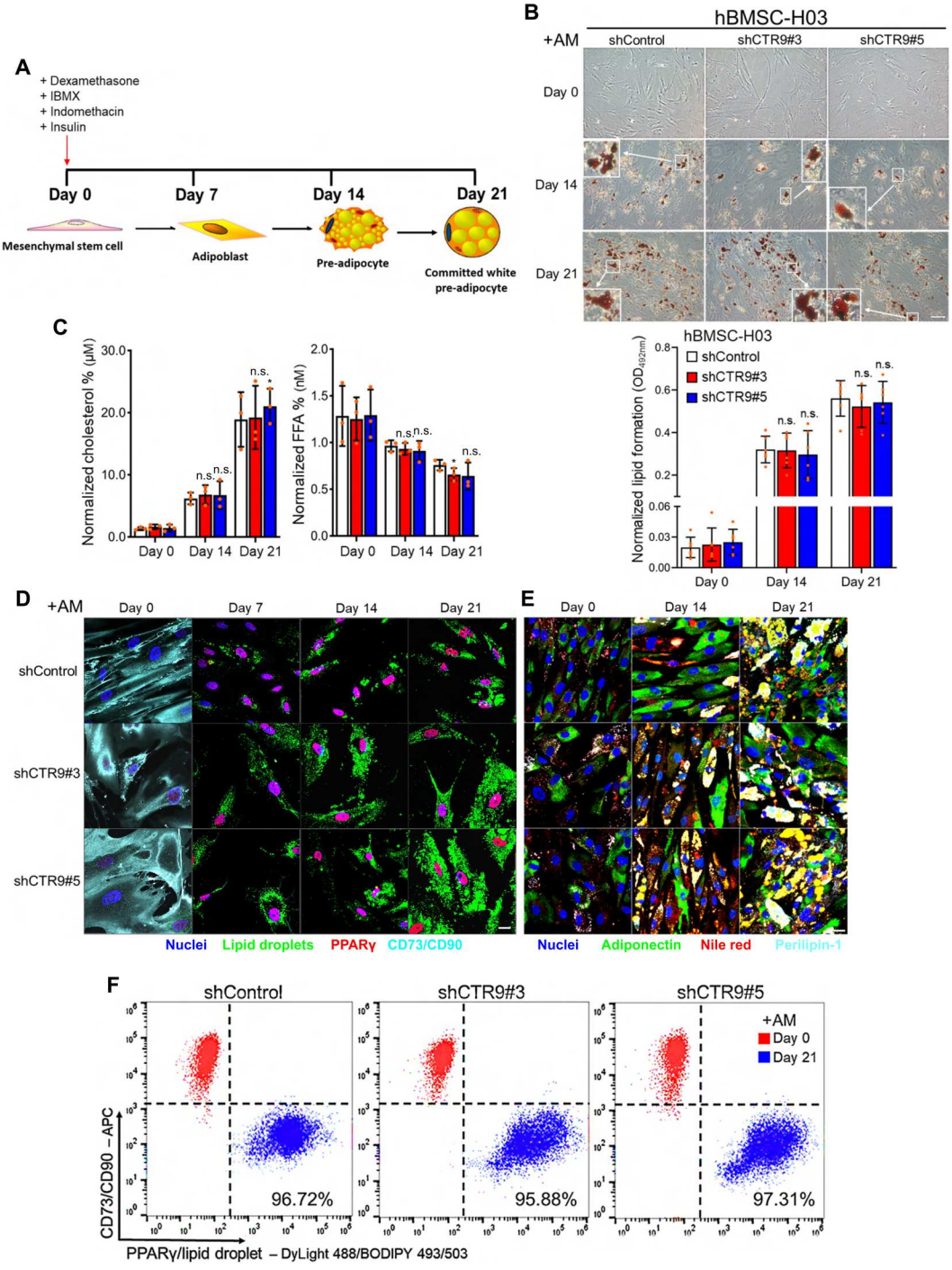

Fig. 6. hMSC adipogenic differentiation was not affected by loss of CTR9. (**A**) Schematic workflow of adipogenic induction of hMSCs in vitro. (**B**) Top: Representative images showing the lipid vesicles formation with Oil Red O staining on shControl or shCTR9 hMSCs (shCTR9#3/#5) after 0 to 21 days of adipogenic induction. Scale bar, 20× (at the bottom right applied to all images). AM, adipogenic induction medium. Bottom: Quantification of lipid vesicles measured by OD_{492nm} absorbance normalized with the respective DNA content. Data are represented as means ± SD ($n = 3$). *P* values were calculated by two-tailed *t* test. (**C**) Quantification of cholesterol and FFA concentration in total lipids extracted from shControl or shCTR9 hMSCs (shCTR9#3/#5) after 0 to 21 days of adipogenic induction. Data normalized by the respective DNA content are represented as means ± SD ($n = 3$). *P* values were calculated by two-tailed *t* test (*$P < 0.05$). (**D**) Immunofluorescence imaging of undifferentiated hMSCs markers CD73/CD90 (cyan), adipogenic-differentiated MSCs marker PPARγ (red), and neutral lipid droplets (green) in shControl or shCTR9 hMSCs (shCTR9#3/#5) after 0 to 21 days of adipogenic induction. Nuclei were stained by Hoechst 33342 in blue. Scale bar, 60× (at the bottom right applied to all images). (**E**) Immunofluorescence imaging of adiponectin (green), Periplin-1 (cyan), and lipid droplets indicated by Nile red in shControl or shCTR9 hMSCs (shCTR9#3/#5) after 0 to 21 days of adipogenic induction. Nuclei were stained by Hoechst 33342 in blue. Scale bar, 60× (at the bottom right applied to all images). (**F**) Flow cytometry analyses of CD73/CD90 and PPARγ/lipid droplet (BODIPY 493/503) in shControl or shCTR9 hMSCs (shCTR9#3/#5) after 0 to 21 days of adipogenic induction.

shCTR9 hMSCs after 14 to 21 days of adipogenic induction. Quantifications of lipid vesicles normalized by DNA are also shown (Fig. 6B, bottom). Similar observations were made using hMSCs originating from different donors (H01/H18) (fig. S6). Cholesterol and free fatty acid (FFA) levels (Fig. 6C), lipid droplets (BODIPY/Nile red) staining, and detection of PPARγ (Fig. 6D), perilipin 1 (cyan; a lipid droplet protein), and adiponectin (green) (Fig. 6E) by immunofluorescence showed that CTR9 depletion did not affect the adipogenic differentiation of hMSCs. These results were confirmed by fluorescence-activated cell sorting analyses of undifferentiated markers CD73/CD90 and PPARγ (Fig. 6F), documenting the gradual loss CD73/CD90 and gain of PPARγ, indicative of the success of MSC differentiation to adipocytes after 14 to 21 days of adipogenic induction. Collectively, our data suggest that CTR9 is dispensable for adipogenic differentiation of hMSCs.

BMP-2 is a downstream effector of CTR9 governing osteochondrogenic differentiation

Our loss- and gain-of-function studies reveal that CTR9 regulates hMSC differentiation to osteoblasts and chondrocytes, but not adipocytes. To identify potential downstream factors regulated by CTR9 during early osteoblast differentiation, we harvested mRNAs from shControl and shCTR9 hMSCs after short-term (7 days) osteogenic induction (Fig. 7A) for bulk RNA sequencing (RNA-seq) and identified 760 differentially expressed genes, whose expression are CTR9 dependent. Among them, 676 genes including *CTR9* itself and osteogenic markers such as *RUNX2*, *BMP2*, *SMAD4*, *ALPL*, and *COL1A1*/*COL1A2* were significantly down-regulated by CTR9 depletion (Fig. 7B). Biological pathway analysis reveals that those down-regulated genes were significantly enriched in bone mineralization–related Gene Ontology (GO) terms, such as positive regulation of bone mineralization and osteoblastic differentiation (fig. S7A). Moreover, mouse analogs of 676 down-regulated genes in hMSCs are predicted to elicit skeletal anomalies and other osteogenesis imperfecta-related disorders in mouse (fig. S7B), implying the high hierarchy of CTR9 in regulating the early onset of bone and cartilage formation.

To reveal the downstream effector of CTR9 in early osteoblast differentiation, we performed Reactome pathway prediction analysis of 676 down-regulated genes (Fig. 7C). Canonical BMP-SMAD pathway represents the top signaling pathway affected by CTR9 KD using gene set enrichment analysis analysis (Fig. 7D), consistent with significant decrease of *BMP-2* in CTR9 KD MSCs (Fig. 7B), implying that BMP-2 is a target of CTR9 during early osteogenesis. BMP-2 maturation requires proteolytic cleavage in ER and Golgi before extracellular secretion in a mature form (*50*–*52*). To assess whether expression and subcellular localization of BMP-2 are affected by CTR9, we performed BMP-2 immunofluorescence staining and WB of BMP-2 in subcellular fractions of control and CTR9 KD MSCs, respectively. Both immunofluorescence staining (Fig. 7E) and WB (Fig. 7F) showed that BMP-2 is trapped in nuclei in CTR9 KD MSCs as compared to cytoplasmic- and membrane-bound BMP-2 in control MSCs, indicating a defect in propeptide cleavage or the extracellular secretion of BMP-2. Upon osteogenic induction for 3 days, BMP-2 (red) is largely synthesized around the ER, and then prematured BMP-2 protein are cleaved at the ER outer membrane (calnexin is an ER membrane marker; green) and Golgi before extracellular secretion after 7 to 14 days (*52*, *53*). These processes are prerequisite for BMP-2 association with its receptors on the cellular membrane (1,1-Dioctadecyl-3,3,3,3-tetramethylindodicarbocyanine [DiD]) to stain cytoplasmic and nuclear membrane; cyan) where downstream signal cascade is activated (Fig. 7E) (*12*, *53*). Extraction of membrane-associated BMP-2 (Fig. 7F) for WB and ELISA (fig. S7C) showed a delayed BMP-2 secretion in CTR9 KD as compared with control KD hMSCs after 7 to 21 days of osteogenic induction.

BMP-2 activation is signified by elevated phosphorylation of SMAD1/5/8 and nucleus translocation of SMAD4 (*54*, *55*). Phosphorylation of SMAD1/5 and SMAD4 nuclear localization were observed in control KD hMSCs after 7 to 21 days of osteogenic induction, whereas these processes were compromised in CTR9 KD hMSCs (fig. S7D). Concomitantly, BMP-2 downstream targets including osteomodulin (*56*), collagen type II (*57*), and Osterix (*58*–*60*) were not induced in CTR9 KD hMSCs to comparable levels as in control KD group (fig. S7E).

We next determined whether supplementing recombinant BMP-2 peptide in osteoconductive medium can rescue the osteogenic or chondrogenic defects in CTR9 KD MSCs. Figure 7G showed that supplementing BMP-2 recombinant peptide in osteoconductive medium increased ALP activity and calcium deposition in shControl hMSCs and partially rescued the osteogenic defects in shCTR9 MSCs. However, adding BMP-2 recombinant peptide to normal growth medium [minimum essential medium α (MEMα)] has no effect on osteogenesis (+OM day 0), suggesting that BMP-2 alone is necessary but not sufficient for osteogenic induction. Similarly, addition of BMP-2 recombinant peptide in the chondrogenic induction medium alleviated the defects in GAG (*16*) deposition and collagen fibrosis caused by CTR9 KD. In shControl hMSCs, supplementing BMP-2 peptide could further promote the chondrogenic capability (fig. S7F). Together, our results demonstrate that BMP-2 is a potent downstream effector of CTR9 to promote osteoblastic and chondrogenic initiation.

H3K27me3-dependent epigenetic mechanisms underlying CTR9-regulated hMSC osteogenesis

Accumulating evidence suggests that H3K27me3 levels play an essential role in modulating the equilibrium between osteogenesis and adipogenesis in hMSCs (*28*, *30*, *61*, *62*). CTR9 KD resulted in a remarkable increase of bulk H3K27me3 levels as shown by immunofluorescence in hMSCs (Fig. 1B). This implies that CTR9 regulates osteogenesis, at least in part, through epigenetic mechanisms engaging H3K27me3. A recent clinical trial combined EZH2 inhibition with a reduced dose of BMP-2 in vivo for bone regeneration, thus minimizing the adverse effects associated with high doses of BMP-2 (*63*). GSK-246, the EZH2 inhibitor, stimulated the osteogenic differentiation of MSCs on 3D scaffolds in vitro, when implanted in vivo, and enhanced vascularization and bone formation (*31*). Accordingly, suppression of H3K27me3 using EZH2 inhibitors may reverse osteogenesis defects by CTR9 KD in hMSCs. To assess this hypothesis, both shControl and shCTR9 hMSCs were treated with increasing concentrations of UNC1999, an EZH2 inhibitor. UNC2400, a structural paralog, and dimethyl sulfoxide (DMSO) served as negative and background controls, respectively. As shown by ALP activity during osteogenic induction, UNC1999 treatment increased osteogenesis in the shControl group and partially rescued the early osteogenic defects in the shCTR9 group, whereas treatment with UNC2400 or DMSO had no effect (Fig. 8A). The quantification of ALP activity was shown in

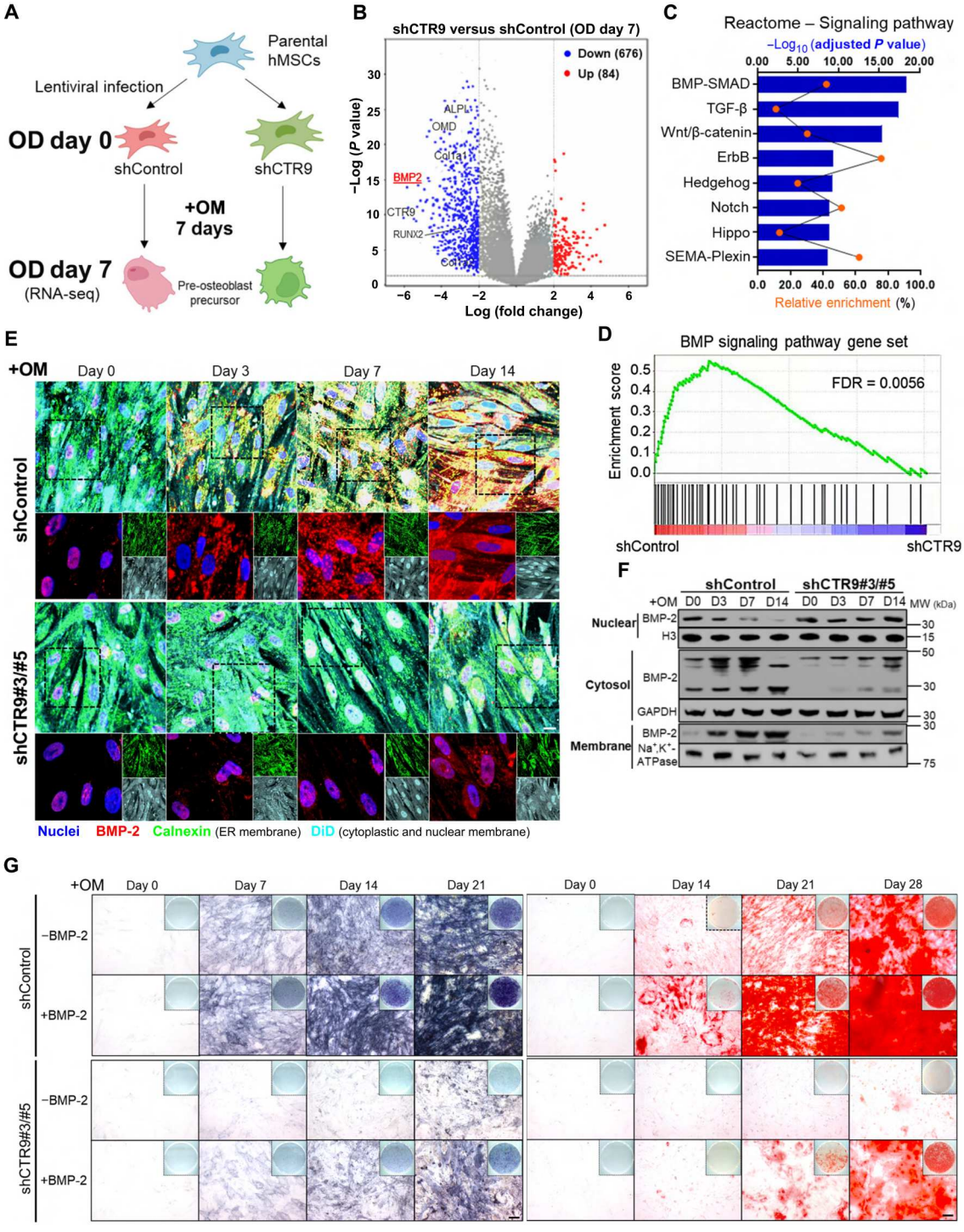

Fig. 7. BMP-2/SMAD pathway was impaired in CTR9 KD hMSCs during osteogenic differentiation. (**A**) Schematic workflow for preparation of shControl and shCTR9 hMSCs to RNA-seq. (**B**) Volcano plots of RNA-seq data showing the up- or down-regulated genes in shCTR9 hMSCs in compared to shControl hMSCs after 7 days of osteogenic induction. Blue dots indicated the significantly down-regulated genes. Red dots indicated the significant upregulated genes (n = 3). (**C**) Reactome pathway analysis of significant down-regulated genes in shCTR9 hMSCs. (**D**) Gene set enrichment analysis analysis of significant down-regulated genes on BMP signaling pathway. FDR, false discovery rate. (**E**) Immunofluorescence staining of BMP-2 (Red) along with the ER marker calnexin (green) and cell/nuclear membrane dye (DiD; cyan) in shControl or shCTR9 hMSCs from days 0 to 14 of osteogenic induction. Scale bar, 60× (at the bottom right applied to all images with merged colors). (**F**) WB of BMP-2 in different cellular fractions derived from shControl or shCTR9 hMSCs after 0 to 14 days of osteogenic induction. Histone H3, GAPDH, and Na^+,K^+-ATPase (Na+- and K+-dependent ATPase) served as loading controls for corresponding cellular fractions. (**G**) Representative images showing the ALP activity–associated BCIP-NBT staining (left) and Alizarin Red S staining of ECM formation (right) in shControl or shCTR9 hMSCs with or without the supplement of BMP-2 peptide after indicated days of osteogenic induction. Scale bar, 20× (at the bottom right applied to all images).

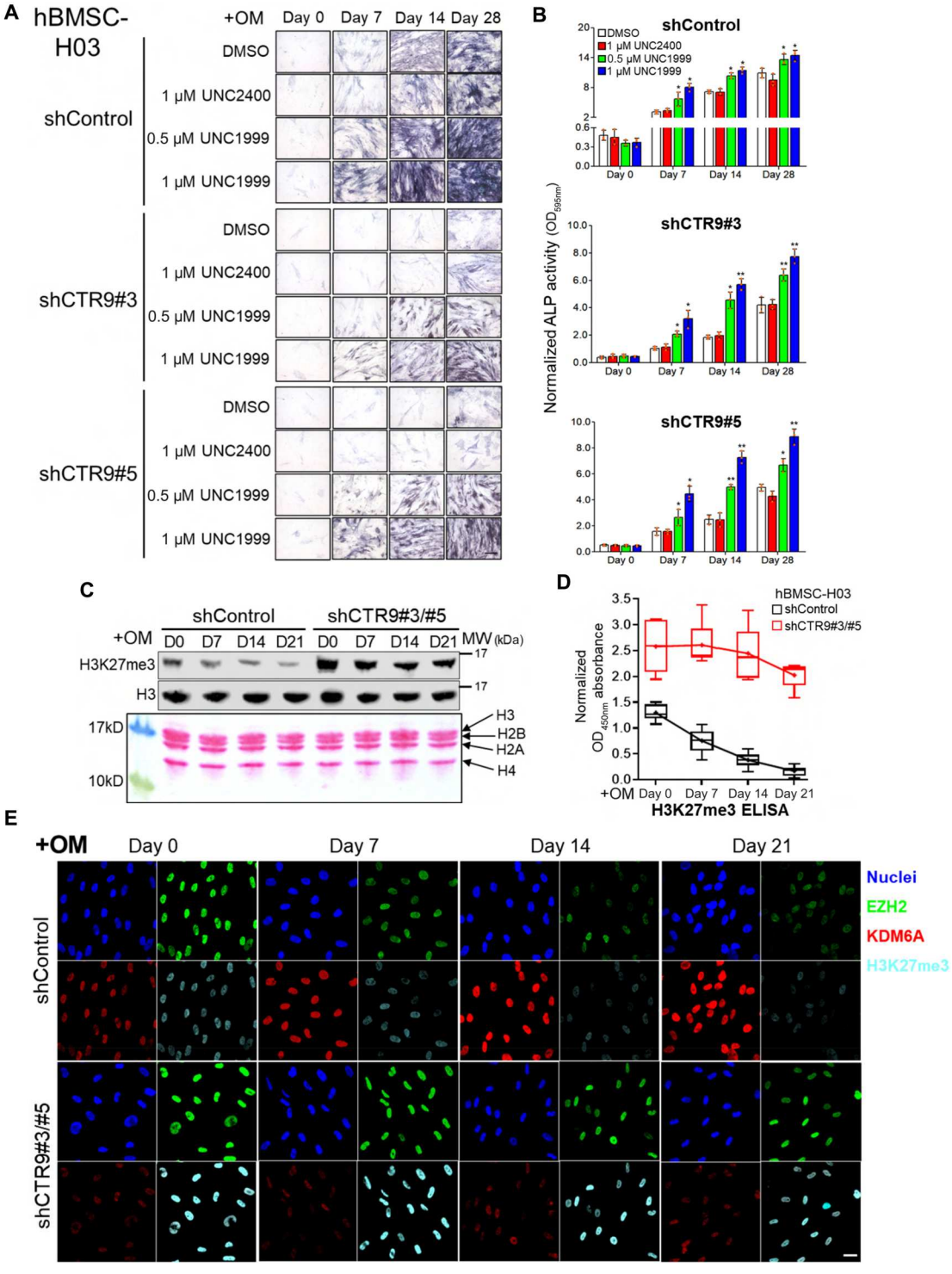

Fig. 8. The osteogenic differentiation defects by loss of CTR9 were rescued by an EZH2 inhibitor. (**A**) Representative images showing the ALP activity–associated BCIP-NBT staining (violet blue) on shControl or shCTR9 hMSCs (shCTR9#3/#5) treated with DMSO, 1 μM UNC2400, or 0.5/1 μM UNC1999 during 0 to 28 days of osteogenic induction. (**B**) Quantification of ALP activities in the respective conditions of (A). Data are represented as means ± SD (n = 3). P values were calculated by two-tailed t test with $*P < 0.05$ and $**P < 0.01$. (**C**) WB analysis of H3K27me3 levels in shControl or shCTR9 hMSCs (shCTR9#3/#5) after 0 to 21 days of osteogenic induction (top). Ponceau S staining of histones (bottom). Each sample is loaded in twofold dilution. Total histone H3 served as a loading control. (**D**) H3K27me3 levels in shControl or shCTR9 hMSCs (shCTR9#3/#5) after 0 to 21 days of osteogenic induction measured by ELISA assays. Data were normalized to the respective total histone H3 levels and shown in minimum to maximum box blot (+, mean; error bars, SD; $n = 6$). (**E**) Immunofluorescence imaging of EZH2 (green), KDM6A (red), and H3K27me3 (cyan) in shControl or shCTR9 hMSCs from days 0 to 21 of osteogenic induction. Nuclei were stained by Hoechst 33342 in blue. Scale bar, 60× (at the bottom right applied to all images).

Fig. 8B. To investigate whether CTR9 counteracts EZH2 activity in hMSCs and regulates H3K27me3 dynamics during osteogenic differentiation, we measured H3K27me3 levels of acid-purified histones in CTR9 KD and control KD hMSCs during 21-day osteogenic differentiation. Western blot analysis (Fig. 8C) and ELISA assay (Fig. 8D) indicates that H3K27me3 levels decreased during osteogenic differentiation in control KD hMSCs. In contrast, the basal level of H3K27me3 was elevated in CTR9 KD hMSCs, and the levels were sustained during 21-day osteogenic induction. These observations were further reinforced by immunofluorescence imaging of H3K27me3/EZH2/KDM6A (Fig. 8E). In control KD hMSCs, EZH2 (H3K27me3 writer) level was decreased and KDM6A (H3K27me3 eraser) level was increased during osteogenic differentiation, which coincided with H3K27me3 level decline. However, in CTR9 KD hMSCs, H3K27me3 levels and EZH2 expression were maintained at prominent levels during osteogenic induction process, whereas KDM6A was weakly induced (Fig. 8E). The decrease of EZH2 expression and H3K27me3 levels and increase of KDM6A expression during osteogenic reprogramming is consistent with the published literature that EZH2-KDM6A axis is the key epigenetic event during osteogenic differentiation of hMSCs (*30*, *64*). The lack of gradual decline of EZH2 and H3K27me3 as well as the increment of KDM6 after osteogenic induction in CTR9 KD hMSCs suggest that CTR9 plays a vital role in epigenetic reprogramming by controlling the H3K27me3 level in hMSCs. Our data support the notion that CTR9-governed osteogenic differentiation of hMSCs is regulated, at least in part, by an epigenetic mechanism engaging enzymes controlling H3K27me3.

DISCUSSION

We phenotypically examined the roles of CTR9 in regulating lineage specification of hMSCs. Knocking down CTR9 in hMSCs selectively affected osteogenic and chondrogenic but not adipogenic differentiation, whereas cell viability and other stem cell properties were not substatially affected. Our in vitro osteogenic induction of hMSCs revealed that loss of CTR9 affects both early and late osteogenic differentiation. CTR9 KD also impairs the formation of cartilage matrix and reduces the expression of key chondrogenic markers, including SOX9, COL2A1, and aggrecan. On the contrary, CTR9 KD in hMSCs did not affect adipogenesis. Moreover, we identified BMP-2 as a major downstream effector of CTR9 in early osteogenesis and chondrogenesis and showed that CTR9-dependent osteochondral differentiation is epigenetically regulated by EZH2 and H3K27me3.

The effects of CTR9 on osteochondral differentiation are in conformality with the expression of lineage-specific markers by RT-PCR and immunofluorescence staining. For example, RUNX2/Osterix mRNA and protein levels were decreased in shCTR9 hMSCs as compared to shControl hMSCs during osteogenic induction (fig. S2D). Furthermore, our RNA-seq analyses comparing shControl and shCTR9 MSCs during the early osteogenesis leads to identification of BMP/SMAD pathway regulated by CTR9 (Fig. 7C). While BMP-2 could partially rescue the defect of CTR9 KD in hMSCs during osteogenic differentiation, additional TFs and regulators may be regulated by CTR9 as well. A thorough transcriptomic profiling of shControl and shCTR9 hMSCs throughout osteogenic or adipogenic induction could better delineate transcriptional networks of pro-osteogenic TFs and signaling pathways that temporally activate osteogenic gene program.

We have shown that expression and secretion of BMP-2 are impaired in CTR9 KD hMSCs, and supplementing BMP-2 to osteogenic and chondrogenic induction medium partially rescues the osteogenic and chondrogenic defects caused by CTR9 KD (Fig. 7 and fig. S7). These results suggest that BMP-2 might be transcriptionally regulated by CTR9, especially at the onset of osteogenic commitment stage. A recent study reports that the acute epigenetic alteration, involving reciprocal gain of H3K4me3 and loss of H3K27me3, occurred on *BMP-2* gene during *Ras*-induced cell senescence (*65*, *66*). Moreover, co-administration of BMP-2 peptide with the EZH2 inhibitor promote differentiation of murine osteoblasts, suggesting that BMP-2 is epigenetically regulated by EZH2 (*31*). We have recently shown that CTR9 counteracts EZH2 activity in breast cells (*38*). Loss of CTR9 resulted in PRC2 subtype switch and expansion of H3K27me3 repressive domains on chromatin (*38*). We thus surmise that BMP-2 is subjected to EZH2/H3K27me3 repression in hMSCs. Upon osteogenic induction, CTR9 releases the repressive H3K27me3 marker on BMP-2, leading to activation of BMP-2 signaling in osteogenic progenitor cells. This model is supported by our finding that the osteogenic defects associated with CTR9 KD hMSCs could be partially rescued by an EZH2 inhibitor (Fig. 8, A and B) and sustained high H3K27me3 levels during osteogenic induction when CTR9 was lost (Fig. 8, C to E), suggesting that PRC2-H3K27me3 mechanisms are conserved in different biological processes and govern CTR9-mediated osteogenic differentiation. Our finding is consistent with published work that inhibition or depletion of EZH2 enhanced osteogenesis (*30*, *31*, *61*, *67*). However, the differential requirement of EZH2 and CTR9 in adipogenic differentiation of hMSCs (i.e., EZH2 promotes adipogenesis whereas CTR9 has no effect) implies that the EZH2-H3K27me3 axis does not account for all biological effects of CTR9. Therefore, profiling of chromatin-bound histone markers (e.g., H3K4me3 and H3K27me3) and PRC2 subunits over the course of osteogenesis or adipogenesis will reveal additional epigenetic players in lineage-specific differentiation.

While CTR9 is not an essential gene in *Saccharomyces cerevisiae* (*68*), CTR9 knockout causes early embryonic lethality in higher eukaryotic organisms such as *Drosophila*, zebrafish, and mouse (*34*, *69*, *70*). The preimplantation defects associated with CTR9 loss resemble the phenotypes in mice that result from lacking core PRC2 subunits SUZ12, EZH2, and Embryonic Ectoderm Development (EED) (*34*). Although the function of CTR9 in mouse skeletal development has not been investigated, we observed colocalization of CTR9 with skeletal muscular progenitor marker HoxA11 (*71*, *72*) in early embryonic stage (unpublished), warranting further study of CTR9 in determining skeletal differentiation in vivo. Furthermore, CTR9 single-nucleotide polymorphisms were found associated with osteoporosis-related Kashin-Beck disease (*37*). Thus, the pathological roles of CTR9 mutations and aberrant expression of CTR9 in bone disorders worth further investigation.

The mechanistic understanding of MSC osteogenic and chondrogenic differentiation are of utmost importance to elucidate their roles in maintaining postnatal tissue homeostasis of mesodermal lineage. Lineage-specific differentiation requires not only lineage-specific TFs but also epigenetic modulators. As lineage-specific TFs are hard to target, great stride has been made to

pharmacologically modulate epigenetic enzymes. We found that either pharmacological inhibition of EZH2 or administrating recombinant BMP-2 peptide partially rescues the osteogenic defects of CTR9 loss, both mimic CTR9 protein restoration. The dual delivery of reduced amounts of BMP-2 and EZH2 inhibitor has recently been applied for treating bone defects with moderate adverse effects (i.e., heterotopic bone formation and acute inflammation) (*63*, *73*, *74*). CTR9 appears to bridge the epigenetic enzymes (i.e., EZH2) and osteoconductive ligands (e.g., BMP-2) in osteogenic differentiation of hMSCs. The mechanism-based therapy holds great promise for treatment of a variety of skeletal disorders. In-depth elucidation of the regulatory network of CTR9 will uncover more therapeutic targets and improve treatment efficacy for bone and cartilage diseases.

MATERIALS AND METHODS

Culture of human MSCs

hMSCs in this study were isolated from the bone marrow of three consenting donors in early passage (H01/H03/H18, p3/p4). hMSCs from each donor were cultured and assayed independently. Isolated hMSCs were cultured in basal medium composed of low-glucose MEMα (Corning), 10% fetal bovine serum (FBS; VWR), and 1% antibiotics (penicillin-streptomycin, Gibco, Thermo Fisher Scientific) and maintained at 37°C under a humidified atmosphere of 5% CO_2. When reaching over 90% confluency, cells were trypsinized using TrypLE Express Enzyme (Thermo Fisher Scientific) and replated at 1000 cells/cm^2. Cell culture medium was changed twice a week. Senescent hMSCs over seven passages will be discarded.

Animal experiment

The in vivo study was performed upon animal protocol approval by the University of Wisconsin-Madison Institutional Animal Care and Use Committee. To evaluate bone formation capability, hMSCs (10^6 cells/cm^3; shControl/shCTR9#3/#5) were preseeded on the 3D Insert PCL scaffold (3D BioTek) for ectopic implantation. The hMSC cell ladens were subcutaneously implanted into the groin of 11- to 12-week-old severe combined immunodeficiency diseased (SCID) mice (NOD.Cg-Prkdc^{scid}I12rg^{tm1wj1}/SzJ) (the Jackson Laboratory). Briefly, scaffolds were inserted into 10-mm incision in mouse and collected after 8 weeks for processing.

Stable CTR9 KD or overexpression in hMSCs

CTR9 was stably knocked down or overexpressed in hMSCs using lentivirus following our established protocol (*38*). hMSCs were selected with puromycin (2 μg/ml) for at least 1 week or sorted for high GFP$^+$ to generate stable CTR9 KD or CTR9-overexpressing hMSCs, respectively. shCTR9#3/#5 are cells separately infected with either shCTR9#3 or shCTR9#5 lentiviral shRNAs, and two cell populations were pooled after puromycin selection for in vitro differentiation experiments.

In vitro differentiation assay

Expanded hMSCs with shControl and shCTR9#3/#5 were cultured in osteogenic, adipogenic, or chondrogenic medium to induce the lineage-specific differentiation in vitro. For osteogenesis, hMSCs were induced in osteogenic medium composed of 1× MEMα (Corning), 10% FBS, 1% antibiotics, 10 mM β-glycerophosphate, L-ascorbic acid-2 phosphate (50 mg/ml), and 0.1 mM dexamethasone (Sigma-Aldrich) for up to 28 days.

For adipogenesis, hMSCs were induced in adipogenic medium consisting of 1× MEMα, 10% FBS, 1% antibiotics, 1 mM dexamethasone, 0.5 mM 3-isobutyl-1-methylxanthine, and insulin (1 mg/ml) (Sigma-Aldrich) for up to 21 days. For chondrogenesis, 1.5 to 3 × 10^5 cells were centrifuged at 600*g* for 5 min to form a high cell density pellet before induction with chondrogenic medium containing 1× Dulbecco's modified Eagle's medium ([DMEM], high glucose), 1% antibiotics, ITS Premix (Corning), 0.9 mM sodium pyruvate, L-ascorbic acid-2 phosphate (50 mg/ml), L-proline (40 mg/ml), 0.1 mM dexamethasone (Sigma-Aldrich), and TGF-β1 (10 ng/ml) (PeproTech) for 21 days during which the medium was changed every 3 days.

Western blot

The WB analysis was performed essentially as described (*38*).

Protein extraction from cellular membrane

Membrane proteins were extracted using the Mem-PER Plus Membrane Protein Extraction Kit (Thermo Fisher Scientific) according to the manufacturer's protocol. To analyze BMP-2 membrane association, adherent cells were washed with Dulbecco's phosphate-buffered saline (DPBS) three times before incubating with crosslinking reaction buffer (5 mM Sulfo-EGS protein crosslinker in DPBS) for 30 min at room temperature, and then the reaction was quenched for 15 min. BMP-2 was extracted using the Mem-PER Plus Membrane Protein Extraction Kit. Hydroxylamine-HCl (pH 8.5) was added to a final concentration of 1 M and incubated with the protein samples for 4 to 6 hours at 37°C on a rotator to reverse the protein crosslinking. Proteins were concentrated using Amicon Ultra 3K MWCO centrifugal filters (MilliporeSigma) before quantification using the Bradford assay (Bio-Rad).

Human BMP-2 ELISA

Serum-free medium and 1 ml of PBS wash buffer were combined and concentrated using Amicon Ultra 3K MWCO centrifugal filters (MilliporeSigma) at 4°C. Concentrated supernatant was resuspended in 100 μl of ice-cold PBS for measuring the BMP-2 secretion using the Human BMP-2 DuoSet ELISA Kit (R&D Systems).

Total RNA extraction and real-time qPCR

For 2D monolayer culture, the total RNA was extracted from cells using the E.Z.N.A HP Total RNA Extraction Kit (Omega) under the manufacturer's protocol. For 3D spheroids, the total RNA was extracted from spheroids using the TRIzol reagent (Invitrogen). The quantity and quality of total RNA were measured using NanoDrop 1000 (Thermo Fisher Scientific) before reverse transcription using the SuperScript First-Strand cDNA Synthesis Kit with 6-nucleotide oligomer random oligos (Invitrogen). The mRNA expression of genes of interest was determined using the iQSYBR Green Premix (Bio-Rad), and the mRNA levels were calculated using the $2^{-\triangle Ct}$ method with reference to the control 18*S* ribosomal RNA. The primer sequences are listed in table S1.

Immunofluorescence staining of cell skeletons in hMSCs

hMSCs with shControl or shCTR9#3/#5 were seeded on 3.5-cm petri dishes with glass bottom. Cells were fixed in 4% formaldehyde

for 15 min and then washed with DPBS three times. Subsequently, cells were permeabilized in 0.3% Triton X-100 in PBS for 10 min, blocked with 3% bovine serum albumin (BSA) in PBST (PBS + 0.1% Triton X-100) for 1 hour, and incubated with tubulin (Thermo Fisher Scientific) at room temperature for 2 hours. Cells were then washed with PBST, followed by incubation with secondary antibody [1:250; fluorescein isothiocyanate (FITC)–goat anti-mouse immunoglobulin G (IgG) (H+L); Bethyl Laboratories] for 45 min at room temperature. After being washed twice in PBST, cells were incubated with 50 nM Alexa Fluor 555 phalloidin (Cell Signaling Technology) and Hoechst 33342 (10 mg/ml; Cell Signaling Technology) at 37°C for 15 min and then washed twice in DPBS. Fluorescence was detected using a Nikon A1R confocal microscope at appropriate wavelengths at the University of Wisconsin–Madison Imaging Core.

Cell cycle profiling and senescence-associated β-galactosidase staining

To assess the cell cycle distribution, hMSCs were trypsinized, fixed in cold 95% ethanol, and washed in PBS. The fixed cells were then resuspended in PI staining solution [ribonuclease A (200 μg/ml), PI (50 μg/ml), 0.1% (v/v) Triton X-100 in PBS, and 1% BSA] and incubated overnight at 4°C. Samples were analyzed at the University of Wisconsin Flow Cytometry Laboratory. Data were analyzed using FlowJo software (version 10, Tree Star). For β-galactosidase staining, cells were fixed in a 2% formaldehyde/0.2% glutaraldehyde solution for 5 min followed by X-Gal staining at 37°C overnight.

3D spheroid formation

hMSCs (~2×10^5) were resuspended in ~250 μl of MEMα medium, seeded in 96-well round bottom plates with ultralow attachment (Corning), and centrifuged at 500*g* for 10 min. 3D spheroid cultures were grown at 37°C with 5% CO_2. Bright-field images were taken within 48 hours after cell seeding on a Leica Quick-Check inverted microscopy. 3D spheroids were harvested after 72 hours and subjected to histological evaluation.

Annexin V and PI staining

Annexin V and PI staining were analyzed by flow cytometry following the manufacturer′s protocol. (eBioscience, Annexin V Apoptosis Detection Kit FITC, Invitrogen).

BCIP-NBT substrate staining (ALP activity)

For 2D monolayer culture, MSCs were fixed in formalin for 2 min, incubated with BCIP-NBT substrate solution for 10 min at dark, and washed with DPBS twice. After image analysis, DNA was extracted from cells for PicoGreen Assay. For 3D ectopic bone formation, a quarter of sectioned scaffolds were fixed with 3.7% formaldehyde for 5 min, stained with BCIP-NBT staining solution for 15 min, followed by PBST wash and acquisition of digital images of stained scaffolds.

Picrosirius red staining

For 2D monolayer culture, cells were fixed in formalin for 10 min, incubated in 0.1% Picrosirius red solution for 1 hour, followed by washing in 0.5% acetic acid and distilled water before subjected for bright-field imaging. For 3D spheroids or 3D ectopic bone formation, deparaffinized spheroid or scaffold sections were rehydrated. Nuclei were stained with Weigert′s hematoxylin (Sigma-Aldrich), and collagen was stained in Picrosirius red solution.

Alizarin Red S staining

For 2D monolayer culture, cells were fixed in 60% isopropanol and stained with Alizarin Red S staining solution [Alizarin Red S (20 mg/ml), pH 4.1 to 4.3, 0.22 μm filtered] for 45 min in the dark. For scaffolds, a quarter of scaffolds were fixed with 3.7% formaldehyde at 37°C for 24 hours and then stained with Alizarin Red S (10 mg/ml).

Human osteocalcin/osteopontin ELISA

For 2D monolayer culture, serum-free medium supernatant as well as 1 mL PBS that rinsed with monolayer surface were collected and concentrated using a Amicon Ultra 3K MWCO Centrifugal Filters (Millipore Sigma) at 4°C. Concentrated supernatant was resuspended in ice-cold PBS in a final volume of 100ul. For scaffolds, a quarter of scaffolds were rinsed with PBS and frozen until assay. Thawed scaffolds were incubated in 0.5 mL of 0.5 M HCl for 30 mins at 37? followed by neutraliztion of 1M NaOH. Amount of Osteocalcin or Osteopontin in secrection or extracts were measured by Osteocalcin Human ELISA Kit (Invitrogen) or Human Osteopontin ELISA Kit (Sigma Aldrich) per manufacturer′s protocol, respectively. Genomic DNA extraction from monolayer cell culture or scaffolds followed by Pico Green quantification is used for data normalization.

Oil Red O staining

Oil Red O staining was performed using standard protocol (*61*).

Quantification of cholesterol and FFAs from total lipids

Total lipids were extracted from cells as described (*75*).

Preparation of 3D spheroids embedding FFPE

Cell pellets were fixed in 4% formaldehyde, dehydrated by a series of gradient ethanol, infiltrated with xylene, and then embedded in paraffin. Embedded cell pellets were cut into 8-mm sections with a microtome.

Alcian blue staining

Deparaffinize FFPE slides and rehydrate through a series of gradient ethanol to distilled water at the final. Stain the spheroid sections in Alcian blue solution [Alcian blue 8GX (1 mg/ml; Thermo Fisher Scientific) and 3% acetic acid (pH 2.5)] for 30 min with 2 min rinse in running tap water afterward. Counterstain the sections in nuclear fast red solution [nuclear fast red (1 mg/ml; Sigma-Aldrich), 5% aluminum sulfate (Fisher Scientific), 0.8 μm filtered, and 1% thymol preservative (Sigma-Aldrich) added]. Wash the slides in running tap water for 1 min. Dehydrate the slides through 70 to 100% ethanol and clear in xylene. Coverslip the slides with resinous mounting medium at last.

Toluidine blue staining

Deparaffinize FFPE slides and rehydrate through a series of gradient ethanol to distilled water at the final. Stain the spheroid sections in toluidine blue working solution [toluidine blue O (1 mg/ml; Sigma-Aldrich), 7% EtOH, and 1% NaCl (pH 2.3 to 2.5)] for 3 min with three times wash of distilled water afterward. Quickly dehydrate the

slides through 70 to 100% ethanol and clear in xylene. Coverslip the slides with resinous mounting medium at last.

DMMB staining

Deparaffinize FFPE slides and rehydrate through a series of gradient ethanol to distilled water at the final. Stain the spheroid sections in DMMB staining solution [0.1% (w/v) dimethyl-methylene blue (Sigma-Aldrich) dissolved in distilled water] for 5 min followed by three times wash of distilled water. Quickly dehydrate the slides through 70 to 100% ethanol and clear in xylene. Coverslip the slides with resinous mounting medium at last.

GAGs quantification

To examine chondrogenic differentiation, cell pellets were digested with papain solution and detected the GAG content with the DMMB assay (Sigma-Aldrich). The total GAG amount was further normalized with the DNA content measured separately by the PicoGreen assay (Thermo Fisher Scientific). All procedures followed the manufacturer's instructions.

ALP histological staining

ALP histological staining was performed using SIGMAFAST Fast Red TR/Naphthol AS-MX Tablets (Sigma-Aldrich) under manufacturer's protocol.

Von-Kossa and Masson's trichome staining

Von-Kossa and Masson's trichome staining were performed as described (*27*, *76*).

Flow cytometry analysis of osteo−/adipogenic markers

For analysis of osteogenic markers, hMSCs were incubated with allophycocyanin (APC)–conjugated CD73/CD90 antibodies (eBioscience) or Alexa Fluor 488–conjugated Osteopontin/Osteocalcin antibodies (Abcam). For adipogenic markers, cells were incubated with APC-conjugated CD73/CD90 antibodies (eBioscience) or DyLight 488–conjugated PPARγ antibody (Cell Signaling Technology) followed by BODIPY 493/503 labeling.

Immunofluorescence staining

For analysis of osteogenic markers, hMSCs were incubated with RUNX2 (rabbit, Cell Signaling Technology) or osteocalcin (mouse, Novus Biologicals) primary antibodies followed by respective FITC-conjugated whole IgG or Cy3-conjugated Fab Fragments secondary antibodies [Alexa Fluor 488 goat anti-rabbit IgG (H+L), Invitrogen; Cy3 AffiniPure Fab Fragment Goat Anti-Mouse IgG (H+L), Jackson ImmunoResearch]. APC-conjugated CD73/CD90 antibodies (mouse, eBioscience) and corresponding secondary antibody [Cy5-goat anti-mouse IgG (H+L), Bethyl Laboratories] were lastly applied.

For analysis of adipogenic markers, cells were simultaneously incubated with PPARγ (rabbit, Cell Signaling Technology) and APC-conjugated CD73/CD90 primary antibodies (mouse, eBioscience), followed by respective secondary antibodies [Cy3-goat anti-rabbit IgG (H+L); Cy5-goat anti-mouse IgG (H+L), Bethyl Laboratories]. Lipid droplets were further stained by 2 μM BODIPY 493/503 at 37°C for 15 min followed by PBS wash.

For analysis of chondrogenic-related markers, paraffin-embedded spheroids are deparaffinized and rehydrated followed by antigen retrieval. After washing in distilled water, sections were permeabilized with 0.25% Triton X-100 in PBS and incubated with primary antibodies and fluorophore-conjugated secondary antibodies.

Cells on scaffolds were fixed with 3.7% formaldehyde for 15 min, washed in DPBS, and permeabilized with 0.2% Triton X-100 for 10 min. Human specific osteocalcin antibody (Novus Biologicals, #MAB1419) and FITC-conjugated secondary antibody [FITC-goat anti-mouse IgG (H+L), Bethyl Laboratories] were used for osteocalcin staining. Alexa Fluor 555–Phalloidin (100 nM in PBS, Invitrogen) and Hoechst (1 μg/ml in PBS buffer, Cell Signaling Technology) were used to stain for F-actin and nuclei, respectively.

Confocal microscopy of scaffolds

Confocal microscopy (Nikon Upright FN1 microscope) was used to measure osteocalcin enrichment and mineralization using scaffolds soaked in DPBS (not air-dried). High-resolution *z*-stack images were captured with a 10×/0.80 air immersion objective (1-mm z-step size) for nuclei (Hoechst, 33342), F-actin (Alexa Fluor 555–Phalloidin), and human specific Osteocalcin (Novus Biologicals; human specific osteocalcin antibody).

Ectopic bone formation measured by micro-CT

hMSCs ($1 \times 10^6/cm^3$) were induced with osteoinduction medium for 7 days in vitro, embedded into 3D PCL scaffolds, followed by implanting subcutaneously into the dorsal surface of 8- to 10-week-old male non-obese diabetic (NSD) mice. The whole mice were subjected to in vivo micro-CT scanning after 4 or 8 weeks of implantation using Inveon hybrid microPET/CT scanner (Siemens). The region of interest (ROI) of the implanted scaffold was defined for analysis in Inveon Research workspace 4.2 (Siemens Healthineers). Mineralization was evaluated by calculating the volume and intensity of mineralized tissue in the ROI.

RNA-seq and data analyses

The RNA-seq library was prepared using the SMARTer Stranded Total RNA-Seq Kit v2–Pico Input Mammalian Kit (Takara Bio). Qualified libraries were deep-sequenced using an Illumina NextSeq 500 at the Northwestern University (NUseq core). Trimmed RNA sequencing reads were aligned to the transcript annotation of human reference genome (hg38.ncbiRefSeq.gtf) using STAR (v2.7.9a). Duplicated reads and reads with low mapping quality were eliminated by Sambamba tools (v0.7.1). FeatureCounts (subread package, v2.0.1) was used to count reads as a measure of gene expression. Differential expressed genes were identified by DESeq2 (v1.36.0) in R with false discovery rate < 0.05.

Statistical analysis

Statistical comparisons between two groups were performed with GraphPad Prism software 8.0 using an unpaired two-tailed *t* test with a Welch correction or paired two-tailed Student's *t* test. The sample size (*n*) was indicated in the figure legends. Details for data analyses and statistical significance were described in the Materials and Methods or figure legends.

Supplementary Materials

This PDF file includes:

Figs. S1 to S7

Table S1

View/request a protocol for this paper from *Bio-protocol*.

REFERENCES AND NOTES

1. J. Feng, A. Mantesso, C. De Bari, A. Nishiyama, P. T. Sharpe, Dual origin of mesenchymal stem cells contributing to organ growth and repair. *Proc. Natl. Acad. Sci. U.S.A.* **108**, 6503–6508 (2011).
2. L. A. Marquez-Curtis, A. Janowska-Wieczorek, L. E. McGann, J. A. Elliott, Mesenchymal stromal cells derived from various tissues: Biological, clinical and cryopreservation aspects. *Cryobiology* **71**, 181–197 (2015).
3. G. Sheng, The developmental basis of mesenchymal stem/stromal cells (MSCs). *BMC Dev. Biol.* **15**, 44 (2015).
4. T. Hoshiba, N. Kawazoe, G. Chen, The balance of osteogenic and adipogenic differentiation in human mesenchymal stem cells by matrices that mimic stepwise tissue development. *Biomaterials* **33**, 2025–2031 (2012).
5. I. Shur, O. Reish, E. Ezra, D. Benayahu, Analysis of mesenchymal cells derived from an chondrodysplasia punctuate patient and donors. *J. Cell. Biochem.* **93**, 112–119 (2004).
6. H. Choi, T. H. Kim, S. Yang, J. C. Lee, H. K. You, E. S. Cho, A reciprocal interaction between β-catenin and osterix in cementogenesis. *Sci. Rep.* **7**, 8160 (2017).
7. W. G. Jang, E. J. Kim, D. K. Kim, H. M. Ryoo, K. B. Lee, S. H. Kim, H. S. Choi, J. T. Koh, BMP2 protein regulates osteocalcin expression via Runx2-mediated Atf6 gene transcription. *J. Biol. Chem.* **287**, 905–915 (2012).
8. F. Villanueva, H. Araya, P. Briceño, N. Varela, A. Stevenson, S. Jerez, F. Tempio, J. Chnaiderman, C. Perez, M. Villarroel, E. Concha, F. Khani, R. Thaler, F. Salazar-Onfray, G. S. Stein, A. J. van Wijnen, M. Galindo, The cancer-related transcription factor RUNX2 modulates expression and secretion of the matricellular protein osteopontin in osteosarcoma cells to promote adhesion to endothelial pulmonary cells and lung metastasis. *J. Cell. Physiol.* **234**, 13659–13679 (2019).
9. M. S. Madsen, R. Siersbaek, M. Boergesen, R. Nielsen, S. Mandrup, Peroxisome proliferator-activated receptor γ and C/EBPα synergistically activate key metabolic adipocyte genes by assisted loading. *Mol. Cell. Biol.* **34**, 939–954 (2014).
10. A. C. Carreira, G. G. Alves, W. F. Zambuzzi, M. C. Sogayar, J. M. Granjeiro, Bone morphogenetic proteins: Structure, biological function and therapeutic applications. *Arch. Biochem. Biophys.* **561**, 64–73 (2014).
11. A. Cuellar, A. H. Reddi, Cell biology of osteochondromas: Bone morphogenic protein signalling and heparan sulphates. *Int. Orthop.* **37**, 1591–1596 (2013).
12. V. S. Salazar, L. W. Gamer, V. Rosen, BMP signalling in skeletal development, disease and repair. *Nat. Rev. Endocrinol.* **12**, 203–221 (2016).
13. F. Afzal, J. Pratap, K. Ito, Y. Ito, J. L. Stein, A. J. van Wijnen, G. S. Stein, J. B. Lian, A. Javed, Smad function and intranuclear targeting share a Runx2 motif required for osteogenic lineage induction and BMP2 responsive transcription. *J. Cell. Physiol.* **204**, 63–72 (2005).
14. P. O. Editors, Expression of concern: Sox9 potentiates BMP2-induced chondrogenic differentiation and inhibits BMP2-induced osteogenic differentiation. *PLOS ONE* **16**, e0249684 (2021).
15. P. Xiao, Z. Zhu, C. du, Y. Zeng, J. Liao, Q. Cheng, H. Chen, C. Zhao, W. Huang, Silencing Smad7 potentiates BMP2-induced chondrogenic differentiation and inhibits endochondral ossification in human synovial-derived mesenchymal stromal cells. *Stem Cell Res. Ther.* **12**, 132 (2021).
16. S. H. McBride-Gagyi, J. A. McKenzie, E. G. Buettmann, M. J. Gardner, M. J. Silva, Bmp2 conditional knockout in osteoblasts and endothelial cells does not impair bone formation after injury or mechanical loading in adult mice. *Bone* **81**, 533–543 (2015).
17. J. Feng, G. Yang, G. Yuan, J. Gluhak-Heinrich, W. Yang, L. Wang, Z. Chen, J. Schulze McDaniel, K. J. Donly, S. E. Harris, M. MacDougall, S. Chen, Abnormalities in the enamel in bmp2-deficient mice. *Cells Tissues Organs* **194**, 216–221 (2011).
18. F. Guo, J. Feng, F. Wang, W. Li, Q. Gao, Z. Chen, L. Shoff, K. J. Donly, J. Gluhak-Heinrich, Y. H. P. Chun, S. E. Harris, M. MacDougall, S. Chen, Bmp2 deletion causes an amelogenesis imperfecta phenotype via regulating enamel gene expression. *J. Cell. Physiol.* **230**, 1871–1882 (2015).
19. E. J. Jin, S. Y. Lee, Y. A. Choi, J. C. Jung, O. S. Bang, S. S. Kang, BMP-2-enhanced chondrogenesis involves p38 MAPK-mediated down-regulation of Wnt-7a pathway. *Mol. Cells* **22**, 353–359 (2006).
20. E. P. Ramly, A. R. Alfonso, R. S. Kantar, M. M. Wang, J. R. D. Siso, A. Ibrahim, P. G. Coelho, R. L. Flores, Safety and efficacy of recombinant human bone morphogenetic protein-2 (rhBMP-2) in craniofacial surgery. *Plast. Reconstr. Surg. Glob. Open* **7**, e2347 (2019).
21. J. Even, M. Eskander, J. Kang, Bone morphogenetic protein in spine surgery: Current and future uses. *J. Am. Acad. Orthop. Surg.* **20**, 547–552 (2012).
22. B. Skovrlj, A. Marquez-Lara, J. Z. Guzman, S. A. Qureshi, A review of the current published spinal literature regarding bone morphogenetic protein-2: An insight into potential bias. *Curr. Rev. Musculoskelet. Med.* **7**, 182–188 (2014).
23. E. J. Woo, Recombinant human bone morphogenetic protein-2: Adverse events reported to the manufacturer and user facility device experience database. *Spine J.* **12**, 894–899 (2012).
24. L. D. Loozen, M. C. Kruyt, A. H. M. Kragten, T. Schoenfeldt, M. Croes, C. F. Oner, W. J. A. Dhert, J. Alblas, BMP-2 gene delivery in cell-loaded and cell-free constructs for bone regeneration. *PLOS ONE* **14**, e0220028 (2019).
25. Y. Kong, Y. Zhao, D. Li, H. Shen, M. Yan, Dual delivery of encapsulated BM-MSCs and BMP-2 improves osteogenic differentiation and new bone formation. *J. Biomed. Mater. Res. A* **107**, 2282–2295 (2019).
26. A. Rojas, H. Sepulveda, B. Henriquez, R. Aguilar, T. Opazo, G. Nardocci, F. Bustos, J. B. Lian, J. L. Stein, G. S. Stein, B. Zundert, A. J. Wijnen, M. L. Allende, M. Montecino, Mll-COMPASS complexes mediate H3K4me3 enrichment and transcription of the osteoblast master gene Runx2/p57 in osteoblasts. *J. Cell. Physiol.* **234**, 6244–6253 (2019).
27. H. Sepulveda, R. Aguilar, C. P. Prieto, F. Bustos, S. Aedo, J. Lattus, B. van Zundert, V. Palma, M. Montecino, Epigenetic signatures at the RUNX2-P1 and Sp7 gene promoters control osteogenic lineage commitment of umbilical cord-derived mesenchymal stem cells. *J. Cell. Physiol.* **232**, 2519–2527 (2017).
28. Y. Cao, L. Li, Z. Fan, The role and mechanisms of polycomb repressive complex 2 on the regulation of osteogenic and neurogenic differentiation of stem cells. *Cell Prolif.* **54**, e13032 (2021).
29. P. Wang, Y. Li, T. Meng, J. Zhang, Y. Wei, Z. Meng, Y. Lin, D. Liu, L. Sui, KDM6A promotes chondrogenic differentiation of periodontal ligament stem cells by demethylation of SOX9. *Cell Prolif.* **51**, e12413 (2018).
30. S. Hemming, D. Cakouros, S. Isenmann, L. Cooper, D. Menicanin, A. Zannettino, S. Gronthos, EZH2 and KDM6A act as an epigenetic switch to regulate mesenchymal stem cell lineage specification. *Stem Cells* **32**, 802–815 (2014).
31. A. Dudakovic, R. M. Samsonraj, C. R. Paradise, C. Galeano-Garces, M. O. Mol, D. Galeano-Garces, P. Zan, M. L. Galvan, M. Hevesi, O. Pichurin, R. Thaler, D. L. Begun, P. Kloen, M. Karperien, A. N. Larson, J. J. Westendorf, S. M. Cool, A. J. van Wijnen, Inhibition of the epigenetic suppressor EZH2 primes osteogenic differentiation mediated by BMP2. *J. Biol. Chem.* **295**, 7877–7893 (2020).
32. D. Yang, H. Okamura, J. Teramachi, T. Haneji, Histone demethylase Utx regulates differentiation and mineralization in osteoblasts. *J. Cell. Biochem.* **116**, 2628–2636 (2015).
33. S. B. Van Oss, C. E. Cucinotta, K. M. Arndt, Emerging Insights into the roles of the Paf1 complex in gene regulation. *Trends Biochem. Sci.* **42**, 788–798 (2017).
34. K. Zhang, J. M. Haversat, J. Mager, CTR9/PAF1c regulates molecular lineage identity, histone H3K36 trimethylation and genomic imprinting during preimplantation development. *Dev. Biol.* **383**, 15–27 (2013).
35. P. Onal, D. Grün, C. Adamidi, A. Rybak, J. Solana, G. Mastrobuoni, Y. Wang, H.-P. Rahn, W. Chen, S. Kempa, U. Ziebold, N. Rajewsky, Gene expression of pluripotency determinants is conserved between mammalian and planarian stem cells. *EMBO J.* **31**, 2755–2769 (2012).
36. Y. Aaronson, I. Livyatan, D. Gokhman, E. Meshorer, Systematic identification of gene family regulators in mouse and human embryonic stem cells. *Nucleic Acids Res.* **44**, 4080–4089 (2016).
37. Y. Wen, X. Guo, J. Hao, X. Xiao, W. Wang, C. Wu, S. Wang, T. Yang, H. Shen, X. Chen, L. Tan, Q. Tian, H. W. Deng, F. Zhang, Integrative analysis of genome-wide association studies and gene expression profiles identified candidate genes for osteoporosis in Kashin-Beck disease patients. *Osteoporos. Int.* **27**, 1041–1046 (2016).
38. N. T. Chan, J. Huang, G. Ma, H. Zeng, K. Donahue, Y. Wang, L. Li, W. Xu, The transcriptional elongation factor CTR9 demarcates PRC2-mediated H3K27me3 domains by altering PRC2 subtype equilibrium. *Nucleic Acids Res.* **50**, 1969–1992 (2022).
39. X. Lin, T. Sun, M. Cai, P. Shen, Cell-death-mode switch from necrosis to apoptosis in hydrogen peroxide treated macrophages. *Sci. China Life Sci.* **53**, 1196–1203 (2010).
40. S. Sanfilippo, M. Canis, L. Ouchchane, R. Botchorishvili, C. Artonne, L. Janny, F. Brugnon, Viability assessment of fresh and frozen/thawed isolated human follicles: Reliability of two methods (Trypan blue and Calcein AM/ethidium homodimer-1). *J. Assist. Reprod. Genet.* **28**, 1151–1156 (2011).
41. S. Kwon, Y. Zhang, P. Matthias, The deacetylase HDAC6 is a novel critical component of stress granules involved in the stress response. *Genes Dev.* **21**, 3381–3394 (2007).
42. <Integrated transcriptomic, phenotypic, and functional study reveals tissue-specific immune properties of mesenchymal stromal cells.pdf>.
43. C. D. Hoemann, H. El-Gabalawy, M. D. McKee, In vitro osteogenesis assays: Influence of the primary cell source on alkaline phosphatase activity and mineralization. *Pathol. Biol. (Paris)* **57**, 318–323 (2009).
44. R. Nishimura, K. Hata, T. Matsubara, M. Wakabayashi, T. Yoneda, Regulation of bone and cartilage development by network between BMP signalling and transcription factors. *J. Biochem.* **151**, 247–254 (2012).
45. Y. T. Tsao, Y. J. Huang, H. H. Wu, Y. A. Liu, Y. S. Liu, O. Lee, Osteocalcin mediates biomineralization during osteogenic maturation in human mesenchymal stromal cells. *Int. J. Mol. Sci.* **18**, 159 (2017).
46. Q. Chen, P. Shou, L. Zhang, C. Xu, C. Zheng, Y. Han, W. Li, Y. Huang, X. Zhang, C. Shao, A. I. Roberts, A. B. Rabson, G. Ren, Y. Zhang, Y. Wang, D. T. Denhardt, Y. Shi, An osteopontin-

integrin interaction plays a critical role in directing adipogenesis and osteogenesis by mesenchymal stem cells. *Stem Cells* **32**, 327–337 (2014).
47. Y. Jing, J. Jing, L. Ye, X. Liu, S. E. Harris, R. J. Hinton, J. Q. Feng, Chondrogenesis and osteogenesis are one continuous developmental and lineage defined biological process. *Sci. Rep.* **7**, 10020 (2017).
48. A. W. Robert, B. H. Marcon, B. Dallagiovanna, P. Shigunov, Adipogenesis, osteogenesis, and chondrogenesis of human mesenchymal stem/stromal cells: A comparative transcriptome approach. *Front. Cell Dev. Biol.* **8**, 561 (2020).
49. C. Merceron, S. Portron, M. Masson, J. Lesoeur, B. H. Fellah, O. Gauthier, O. Geffroy, P. Weiss, J. Guicheux, C. Vinatier, The effect of two- and three-dimensional cell culture on the chondrogenic potential of human adipose-derived mesenchymal stem cells after subcutaneous transplantation with an injectable hydrogel. *Cell Transplant.* **20**, 1575–1588 (2011).
50. R. D. Cordner, L. N. Friend, J. L. Mayo, C. Badgley, A. Wallmann, C. N. Stallings, P. L. Young, D. R. Miles, J. G. Edwards, L. C. Bridgewater, The BMP2 nuclear variant, nBMP2, is expressed in mouse hippocampus and impacts memory. *Sci. Rep.* **7**, 46464 (2017).
51. F. Hillger, G. Herr, R. Rudolph, E. Schwarz, Biophysical comparison of BMP-2, ProBMP-2, and the free pro-peptide reveals stabilization of the pro-peptide by the mature growth factor. *J. Biol. Chem.* **280**, 14974–14980 (2005).
52. D. B. Constam, E. J. Robertson, Regulation of bone morphogenetic protein activity by pro domains and proprotein convertases. *J. Cell Biol.* **144**, 139–149 (1999).
53. D. Chen, M. Zhao, S. E. Harris, Z. Mi, Signal transduction and biological functions of bone morphogenetic proteins. *Front. Biosci.* **9**, 349–358 (2004).
54. Y. Zhao, M. Xiao, B. Sun, Z. Zhang, T. Shen, X. Duan, P. B. Yu, X. H. Feng, X. Lin, C-terminal domain (CTD) small phosphatase-like 2 modulates the canonical bone morphogenetic protein (BMP) signaling and mesenchymal differentiation via Smad dephosphorylation. *J. Biol. Chem.* **289**, 26441–26450 (2014).
55. Z. Zhou, J. Xie, D. Lee, Y. Liu, J. Jung, L. Zhou, S. Xiong, L. Mei, W. C. Xiong, Neogenin regulation of BMP-induced canonical Smad signaling and endochondral bone formation. *Dev. Cell* **19**, 90–102 (2010).
56. W. Lin, X. Zhu, L. Gao, M. Mao, D. Gao, Z. Huang, Osteomodulin positively regulates osteogenesis through interaction with BMP2. *Cell Death Dis.* **12**, 147 (2021).
57. T. Gründer, C. Gaissmaier, J. Fritz, R. Stoop, P. Hortschansky, J. Mollenhauer, W. K. Aicher, Bone morphogenetic protein (BMP)-2 enhances the expression of type II collagen and aggrecan in chondrocytes embedded in alginate beads. *Osteoarthr. Cartil.* **12**, 559–567 (2004).
58. M. H. Lee, T. G. Kwon, H. S. Park, J. M. Wozney, H. M. Ryoo, BMP-2-induced Osterix expression is mediated by Dlx5 but is independent of Runx2. *Biochem. Biophys. Res. Commun.* **309**, 689–694 (2003).
59. A. Ulsamer, M. J. Ortuño, S. Ruiz, A. R. G. Susperregui, N. Osses, J. L. Rosa, F. Ventura, BMP-2 induces Osterix expression through up-regulation of Dlx5 and its phosphorylation by p38. *J. Biol. Chem.* **283**, 3816–3826 (2008).
60. T. Matsubara, K. Kida, A. Yamaguchi, K. Hata, F. Ichida, H. Meguro, H. Aburatani, R. Nishimura, T. Yoneda, BMP2 regulates Osterix through Msx2 and Runx2 during osteoblast differentiation. *J. Biol. Chem.* **283**, 29119–29125 (2008).
61. L. Wang, Q. Jin, J. E. Lee, I. H. Su, K. Ge, Histone H3K27 methyltransferase Ezh2 represses Wnt genes to facilitate adipogenesis. *Proc. Natl. Acad. Sci. U.S.A.* **107**, 7317–7322 (2010).
62. S. R. Thornton, V. L. Butty, S. S. Levine, L. A. Boyer, Polycomb repressive complex 2 regulates lineage fidelity during embryonic stem cell differentiation. *PLOS ONE* **9**, e110498 (2014).
63. H. Lui, R. M. Samsonraj, C. Vaquette, J. Denbeigh, S. Kakar, S. M. Cool, A. Dudakovic, A. J. van Wijnen, Combination of BMP2 and EZH2 inhibition to stimulate osteogenesis in a 3D bone reconstruction model. *Tissue Eng. Part A* **27**, 1084–1098 (2021).
64. A. Dudakovic, E. T. Camilleri, C. R. Paradise, R. M. Samsonraj, M. Gluscevic, C. A. Paggi, D. L. Begun, F. Khani, O. Pichurin, F. S. Ahmed, R. Elsayed, M. Elsalanty, M. E. McGee-Lawrence, M. Karperien, S. M. Riester, R. Thaler, J. J. Westendorf, A. J. van Wijnen, Enhancer of zeste homolog 2 (Ezh2) controls bone formation and cell cycle progression during osteogenesis in mice. *J. Biol. Chem.* **293**, 12894–12907 (2018).
65. M. Fujimoto, Y. Mano, M. Anai, S. Yamamoto, M. Fukuyo, H. Aburatani, A. Kaneda, Epigenetic alteration to activate Bmp2-Smad signaling in Raf-induced senescence. *World J. Biol. Chem.* **7**, 188–205 (2016).
66. A. Kaneda, T. Fujita, M. Anai, S. Yamamoto, G. Nagae, M. Morikawa, S. Tsuji, M. Oshima, K. Miyazono, H. Aburatani, Activation of Bmp2-Smad1 signal and its regulation by coordinated alteration of H3K27 trimethylation in Ras-induced senescence. *PLOS Genet.* **7**, e1002359 (2011).
67. A. Dudakovic, E. T. Camilleri, F. Xu, S. M. Riester, M. E. McGee-Lawrence, E. W. Bradley, C. R. Paradise, E. A. Lewallen, R. Thaler, D. R. Deyle, A. N. Larson, D. G. Lewallen, A. B. Dietz, G. S. Stein, M. A. Montecino, J. J. Westendorf, A. J. van Wijnen, Epigenetic control of skeletal development by the histone methyltransferase Ezh2. *J. Biol. Chem.* **290**, 27604–27617 (2015).
68. A. Massoni-Laporte, M. Perrot, L. Ponger, H. Boucherie, A. L. Guieysse-Peugeot, Proteome analysis of a CTR9 deficient yeast strain suggests that Ctr9 has function(s) independent of the Paf1 complex. *Biochim. Biophys. Acta* **1824**, 759–768 (2012).
69. D. Chaturvedi, M. Inaba, S. Scoggin, M. Buszczak, Drosophila CG2469 encodes a homolog of human CTR9 and is essential for development. *G3 (Bethesda)*. **6**, 3849–3857 (2016).
70. T. Akanuma, S. Koshida, A. Kawamura, Y. Kishimoto, S. Takada, Paf1 complex homologues are required for Notch-regulated transcription during somite segmentation. *EMBO Rep.* **8**, 858–863 (2007).
71. K. M. Pineault, J. Y. Song, K. M. Kozloff, D. Lucas, D. M. Wellik, Hox11 expressing regional skeletal stem cells are progenitors for osteoblasts, chondrocytes and adipocytes throughout life. *Nat. Commun.* **10**, 3168 (2019).
72. C. A. Pagani, A. K. Huber, C. Hwang, S. Marini, K. Padmanabhan, N. Livingston, J. Nunez, Y. Sun, N. Edwards, Y. H. Cheng, N. Visser, P. Yu, N. Patel, J. A. Greenstein, H. Rasheed, R. Nelson, K. Kessel, K. Vasquez, A. L. Strong, G. E. Hespe, J. Y. Song, D. M. Wellik, B. Levi, Novel lineage-tracing system to identify site-specific ectopic bone precursor cells. *Stem Cell Rep.* **16**, 626–640 (2021).
73. M. L. Galvan, C. R. Paradise, E. Kubrova, S. Jerez, F. Khani, R. Thaler, A. Dudakovic, A. J. van Wijnen, Multiple pharmacological inhibitors targeting the epigenetic suppressor enhancer of zeste homolog 2 (Ezh2) accelerate osteoblast differentiation. *Bone* **150**, 115993 (2021).
74. A. Dudakovic, E. T. Camilleri, S. M. Riester, C. R. Paradise, M. Gluscevic, T. M. O'Toole, R. Thaler, J. M. Evans, H. Yan, M. Subramaniam, J. R. Hawse, G. S. Stein, M. A. Montecino, M. E. McGee-Lawrence, J. J. Westendorf, A. J. van Wijnen, Enhancer of zeste homolog 2 inhibition stimulates bone formation and mitigates bone loss caused by ovariectomy in skeletally mature mice. *J. Biol. Chem.* **291**, 24594–24606 (2016).
75. F. Liu, F. Ma, Y. Wang, L. Hao, H. Zeng, C. Jia, Y. Wang, P. Liu, I. M. Ong, B. Li, G. Chen, J. Jiang, S. Gong, L. Li, W. Xu, PKM2 methylation by CARM1 activates aerobic glycolysis to promote tumorigenesis. *Nat. Cell Biol.* **19**, 1358–1370 (2017).
76. Y. Xu, Y. Yang, Z. Hua, S. Li, Z. Yang, Q. Liu, G. Fu, P. Ji, Q. Wu, BMP2 immune complexes promote new bone formation by facilitating the direct contact between osteoclasts and osteoblasts. *Biomaterials* **275**, 120890 (2021).

Acknowledgments: We thank X. Liang for assistance of data organization and UWCCC Flow Cytometry Center and Optical Imaging Core for technical support. **Funding:** This work was supported by the National Institutes of Health, National Cancer Institute grant P30CA014520; the University of Wisconsin-Madison, UW Carbone Cancer Center; and the National Institutes of Health grants R01 CA268183 (to W.X.), R01 CA236356 (to W.X.), R01 CA213293 (to W.X.), and R01 AR064803 (to W.J.L). **Author contributions:** W.X. and N.T.C. conceived the project, designed the experiments, analyzed the data, and wrote the manuscript. N.T.C. performed the experiments with assistance from M.-S.L. M.-S.L. performed the animal study for ectopic bone formation assay. N.T.C. performed bioinformatics analyses. Y.W. organized reagents and maintained the animals. J.G. revised the manuscript. W.-J.L. directed the animal experiments. W.X. directed and supervised all aspects of the study. All authors discussed the results and commented on the manuscript. **Competing interests:** The authors declare that they have no competing interests. **Data and materials availability:** All high-throughput next-generation sequencing datasets generated for this paper have been submitted to GEO database (https://www.ncbi.nlm.nih.gov/geo/) through accession number GSE213277. Flow cytometry and RT-qPCR experiments are uploaded to Dryad with identifier DOI: 10.5061/dryad.x95x69pn9. All data needed to evaluate the conclusions in the paper are present in the paper and/or the Supplementary Materials.

Submitted 10 May 2022
Accepted 19 October 2022
Published 16 November 2022
10.1126/sciadv.adc9222